Journal of Fluids and Structures 109 (2022) 103470

Contents lists available at ScienceDirect

Journal of Fluids and Structures

journal homepage: www.elsevier.com/locate/jfs

Wake response downstream of a spanwise-oscillating hemispherical turret

Aaron L. Roeder [a], Stanislav Gordeyev [b,*]

[a] Applied Technology Associates, Albuquerque, NM, 87123, United States of America
[b] University of Notre Dame, Notre Dame, IN, 46556, United States of America

ARTICLE INFO

Article history:
Received 7 May 2021
Received in revised form 19 October 2021
Accepted 3 December 2021
Available online xxxx

Keywords:
Turrets
Wake dynamics
Separated flows
Forced oscillations

ABSTRACT

An experimental Pressure Sensitive Paint (PSP) study of the unsteady pressure fields downstream of and on an oscillating hemispherical turret at subsonic freestream Mach numbers between 0.3 and 0.6 and Reynolds numbers of about 2 million is presented. The oscillating turret consisted of a hemispheric shell, mounted on an aluminum rectangular plate and is designed to oscillate in the spanwise direction at a single frequency, which lies within the frequency range of the dominant wake motion. The resonant-based aero-elastic response of the turret to the flow resulted in intermittent turret oscillations. Pressure fluctuations in the wake were found to be less energetic for the oscillating turret and the size of the recirculating region was increased, compared to the stationary turret. POD-based modal analysis of the pressure fields revealed that the wake dynamics is characterized by global anti-symmetric and symmetric shedding and showed that the oscillating turret primarily suppressed the global anti-symmetric shedding. The analysis of the unsteady forces acting on the turret demonstrated that the oscillating turret reduces the spanwise component of the unsteady force, while keeping other force components mostly unchanged. Intermittent nature of the spanwise force, which is responsible for the intermittent motion of the oscillating turret, was observed and discussed.

1. Introduction and motivation

Hemispherical turrets provide an optimal geometry for maximizing the field-of-regard of airborne laser systems used in a wide variety of adaptive optics and beam control applications. However, when aircraft is instrumented with a turret-based system, turbulent flow around the turret and throughout the wake, characterized by density gradients, induce variations in fluctuating index-of-refraction. Laser light propagated through regions of air containing spatio-temporal variability in index-of-refraction will aberrate the incident beam (Wang et al., 2012; Jumper and Gordeyev, 2017). Thus, the ramifications of aero-optical distortions on hemispherical turrets as beam directors are significant in their effectiveness to potentially degrade the point-and-track capabilities of adaptive-optics systems. To address this issue, many experimental (Gordeyev and Jumper, 2010; Vukasinovic et al., 2013; De Lucca et al., 2013a; Porter et al., 2013; Morrida et al., 2017) and numerical (Ladd et al., 2009; Morgan and Visbal, 2012; Jelic et al., 2013; Coirier et al., 2014; Matthews et al., 2016) studies were conducted to quantify the aero-optical and fluidic performance of turrets.

* Corresponding author.
E-mail address: sgordeye@nd.edu (S. Gordeyev).

https://doi.org/10.1016/j.jfluidstructs.2021.103470
0889-9746/

Since surface-mounted hemispheres also appear in other applications, such as dome-shaped buildings or sensor protrusions on aircraft, the flow field around solid hemispheres were extensively studied (Savory and Toy, 1986; Manhart, 1998; Tavakol et al., 2015; Wood et al., 2016). Briefly, as a subsonic flow goes around a hemisphere, part of the flow accelerates over it until it separates near the apex at the location determined by the state of the boundary layer near the apex. Once the flow separates, it forms a significantly more turbulent shear layer, which folds downward the surface, forming a separation bubble. On both sides of the bubble, a pair of counterrotating "horn" vortices are formed, which convect in the streamwise direction downstream the turret (Gordeyev and Jumper, 2010). The counterrotating nature of the horn vortices creates a downwash effect and initiates the formation of a "quiet valley" in the center of the wake via Biot–Savart induction (Morrida et al., 2016). As flow stagnates at the leading edge of the turret, it also forms a necklace vortex, whose legs travel around both sides of the turret base and convect in the streamwise direction through the wake.

Numerical simulations of the flow over a rough surface hemisphere at $\mathrm{Re_D} = 1.5 \times 10^4$ were performed in Manhart (1998). Using a modal analysis, two types of the wake dynamics were observed. One of them is due to anti-symmetric or alternating shedding of vortical structures from the opposite spanwise sides of the turret. This anti-symmetric shedding had a range of normalized frequencies $\mathrm{St_D} = fD/\mathrm{U}_\infty = 0.15$–$0.2$, where D is the hemisphere diameter and U_∞ is the incoming freestream speed. Another type was identified as a symmetric vortex shedding, with a characteristic frequency of $\mathrm{St_D} = 0.2$–0.5. Intermittent nature of the wake was observed, where a quasi-periodic vortex shedding was disrupted by shorter periods of time where the wake intensity was significantly reduced and no periodic shedding was present. Similar observations and conclusions were made after a joint numerical and experimental studies of the flow over a smooth hemisphere for $\mathrm{Re_D} = 5 \times 10^4$, where the symmetric shedding occurred for $\mathrm{St_D} = 0.23$–0.31, and the anti-symmetric shedding had a typical frequency of $\mathrm{St_D} = 0.16$. A similar frequency range of the wake shedding vortices over a hemisphere of $0.15 \leq St_\mathrm{D} \leq 0.2$ was found in McCarthy et al. (2019) at a similar $\mathrm{Re_D} = 6.36 \times 10^4$. A wavelet analysis of the fluctuating pressure series on and downstream of the hemisphere also revealed an intermittent coherence across the turbulent wake. A distribution of time intervals of significant intermittency was approximated by an inverse Gaussian probability density function with the mean value of time intervals $\sim 50\ D/\ U_\infty$.

All of these studies found the turret wake to be dominated by low frequency, large-scale structures. These large-scale structures create unsteady forces acting on the turret, and could potentially excite unwanted mechanical vibrations inside the optical layout of the turret or induce elastic deformation of the turret itself, adversely affecting beam control system performance. To investigate this issue, unsteady spatially resolved surface pressure fields on and around the turrets were measured using a fast-response pressure sensitive paint, to study the dynamics of the wake and unsteady forces acting on the turret at various subsonic and transonic speeds for realistic flight range of turret Reynolds numbers between 1.2×10^6 and 2.2×10^6 (De Lucca et al., 2013b; Gordeyev et al., 2014; De Lucca et al., 2018b; Gordeyev et al., 2018). A modal analysis (Gordeyev et al., 2014; De Lucca et al., 2018b), and a conditional analysis by Gordeyev et al. (2018) of the surface pressure field on and downstream of the hemispherical turret revealed that the main dynamic mode in the wake is related to an anti-symmetric vortex shedding. The spectral analysis found that the main frequency of this mode is within the normalized frequency range $St_\mathrm{D} = fD/U_\infty = 0.1$–$0.2$, consistent with the observations at lower Reynolds number, mentioned before. The turret wake was also found to contain secondary spanwise symmetric structures which shed off the top of the turret. Consequently, the unsteady forces acting on the turret had a peak in spectra in the same range of frequencies (De Lucca et al., 2013b).

All aforementioned experimental and numerical studies have assumed that the turret surface was rigid and ignored the mechanical vibration of the turret itself. In real applications, however, the turret skin is relatively thin to make the turret assembly lighter. Studies of the flow around a hemisphere with a deformable rubber skin (Wood et al., 2018) demonstrated that even small amplitudes, less than 0.5% of the diameter, of skin deformation reduced turbulence production in the wake and affected the wake shape and topology. The reason for that was found to be the transfer of kinetic energy from the fluid to the deformable structure.

Typically, a turret assembly consists of a hollow shell with various optical and mechanical components, like lenses, mirrors, motors etc, all designed to propagate a focused beam toward a target. In order to move the assembly in the azimuthal direction, the entire assembly is mounted on a rotating shaft with driving motors, see Jumper et al. (2012) for instance. Due to the large vertical size of the turret, the mounting point between the turret assembly and the shaft can be several feet away from the top of the turret. Due to elastic effects, this mount is not absolutely rigid. Turbulent flow around the turret, particularly the dominant anti-symmetric shedding, will produce unsteady forces acting on the entire assembly. As a consequence, the non-rigid mount can result in mechanical vibration of the turret assembly as a whole, potentially causing non-negligible changes of the wake dynamics and consequent modification of aero-optical effects. Also, the mechanical vibration of the turret might induce additional vibrations of different optical components in the optical set-up, resulting in larger jitter on the outgoing beam.

Vortex-induced vibrations of solid bodies, like spanwise cylinders has been extensively studied over many years, see Sarpkaya (2004), Williamson and Govardhan (2004), or Bearman (2011), for instance. The largest oscillations occur, when the natural frequency of the elastically mounted cylinder is close to the vortex shedding frequency, a so-called "locked-in" mechanism. For sufficiently large oscillations, several different vortex formation modes in the wake were observed and extensively studied. For sufficiently rigidly mounted turrets, however, the amplitudes of the flow-induced oscillations are fairly small, on the order of 1% of D or less. In this case, the oscillations will not significantly alter the wake, but rather result in small alterations of the wake and the forces acting on the vibrating turret.

To investigate this problem, in the presented work a hemispherical turret was allowed to oscillate freely in the spanwise direction at a fixed frequency by mounting it on a flexible metal cantilever beam. The oscillating turret system was designed and built such that the dominant oscillation frequency was within the dominant frequency range of the unsteady anti-symmetric shedding, in order to utilize the "lock-in" mechanism and enforce resonance-related oscillation amplitude amplification. For comparison, the turret was also rigidly affixed to the tunnel wall to represent a stationary turret case. The turret and the wake region were both painted with fast-response porous pressure sensitive paint (PSP) in order to collect spatially–temporally resolved surface pressure fields and compare the global pressure fields between the oscillating and stationary cases. Pressure fields on the surface of the turret were also used to compute and analyze the unsteady forces acting on the turret for both cases.

Section 2 discusses the concept of the oscillating turret design along with feasibility studies and mathematical background related to its construction. Section 3 discusses the experimental setup and implementation of the oscillating turret for subsonic wind tunnel testing. Data analysis is given in Section 4, and experimental results are presented and discussed in Section 5. Conclusions are presented in Section 6.

2. Oscillating turret concept

The concept of an oscillating turret, when a rigid hemispherical turret is mounted on a thin rectangular aluminum plate, is schematically shown in Fig. 1(a). The origin of the frame of reference was chosen to be at the center of the hemispherical turret, with the x-axis denoting the streamwise direction, the y-axis denoting the wall normal direction, and the z-axis denoting the spanwise direction. The plate is aligned along the streamwise x-direction, so the turret can only move in the spanwise z-direction. In this investigation transverse oscillating cantilever uniform Euler–Bernoulli beam theory for a beam with tip mass attachment, presented in Erturk and Inman (2011) and Repetto et al. (2012), was used to model, design, and construct an oscillating turret system. The Euler–Bernoulli cantilever bar dynamic equations were used to demonstrate that the plate and turret system behaves as a pendulum and has a dominant oscillating frequency. This frequency depends on the elastic properties of the plate, mechanical dimensions of the plate, and the mass and inertia of the turret. The vibrational response of this system to the input forcing, $F_z(t)$, applied at the free end of the beam, are governed by the following differential equation,

$$m\frac{\partial^2 v(y,t)}{\partial t^2} + \gamma m\frac{\partial v(y,t)}{\partial t} + E\cdot I_p\frac{\partial^4 v(y,t)}{\partial y^4} = 0 \tag{1}$$

The clamped-free boundary conditions for this system are given by

$$\left[E\cdot I_p\frac{\partial^2 v(y,t)}{\partial y^2} + I_t\frac{\partial^3 v(y,t)}{\partial t^2\partial y}\right]_{y=L} = 0, \left[E\cdot I_p\frac{\partial^3 v(y,t)}{\partial y^3} + M_t\frac{\partial^2 v(y,t)}{\partial t^2}\right]_{y=L} = F_z(t), \tag{2}$$

$$v(y=0,t)=0, \left.\frac{\partial v(y,t)}{\partial y}\right|_{y=0} = 0 \tag{3}$$

In this model, $v(y,t)$ describes the local displacement in the z-direction along the plate due to the unsteady forcing in the spanwise direction, E is Young's modulus for aluminum and ρ is the density of the aluminum plate. L is the length of the plate, w is the plate width, h is the plate thickness, $m = \rho wh$ is the plate mass per unit length, $I_p = wh^3/12$ is the moment of inertia of the cross-sectional area of the plate and γ is the damping coefficient of the aluminum plate. $M_t = M_{shell} + M_{disk}$ is the total mass attached at the end of the beam, which consists of a thin plastic turret shell with the mass M_{shell} and an aluminum mounting disk 3 mm thick with the mass M_{disk}. Finally, I_t is the total moment of inertia of the turret shell and the mounting disk about the attachment line $y = L$,

$$I_t = \frac{1}{4}M_{disk}R^2 + \frac{1}{3}M_{shell}R^2$$

Following the approach, outlined in Erturk and Inman (2011) and Repetto et al. (2012), the solution of the Eqs. (1)–(3) was found using the separation of variables and assuming a harmonic response, $v(y,t) = Y(y;\omega)\exp(i\omega t)$, to a unit single harmonic input, $F_z(t) = \exp(i\omega t)$. From the solution, a spectral transfer function, $G(\omega) = Y(y{=}L;\omega)$, between the input harmonic forcing and the resulted harmonic motion of the turret, was calculated to be

$$G(\omega) = G_{steady}\frac{3\left[\sin(\lambda)\cosh(\lambda) - \cos(\lambda)\sinh(\lambda) + \frac{\omega^2 L\cdot I_t}{\lambda E\cdot I_p}(\cos(\lambda)\cosh(\lambda)-1)\right]}{\lambda^3\cdot\Delta}, \tag{4}$$

where

$$\Delta = 1 + \cos(\lambda)\cosh(\lambda) + \frac{\omega^2 L^3\cdot M_t}{\lambda^3 E\cdot I_p}[\cos(\lambda)\sinh(\lambda) - \sin(\lambda)\cosh(\lambda)]$$
$$-\frac{\omega^2 L\cdot I_t}{\lambda E\cdot I_p}[\cosh(\lambda)\sin(\lambda) + \sinh(\lambda)\cos(\lambda)] + \frac{\omega^4 L^4\cdot M_t\cdot I_t}{\lambda^4(E\cdot I_p)^2}[1-\cos(\lambda)\cosh(\lambda)]$$

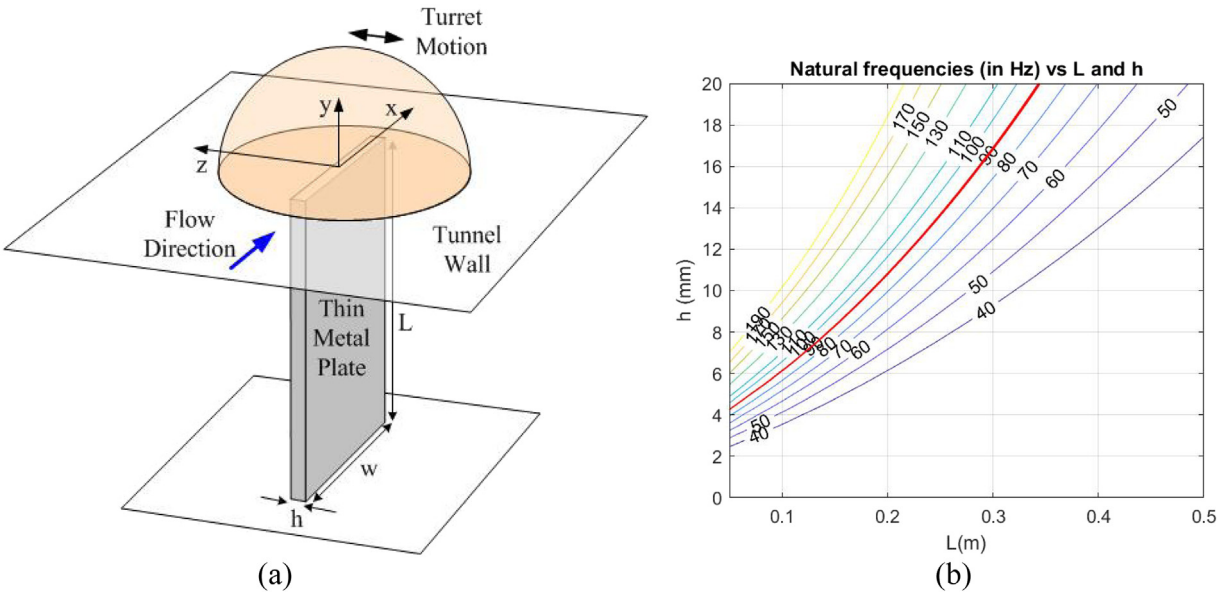

Fig. 1. (a) Schematic of the spanwise-oscillating turret and a frame of reference. (b) Natural frequency of free oscillations for the main vibrational mode of the turret system as a function of plate length, L, and thickness, h. The target frequency line of 90 Hz is indicated in thick red line.

Table 1
Parameters of the oscillating turret system.

Plate Thickness, h	Plate Width, w	Plate Length, L	Plate Moment of Inertia, I_p	Damping coefficient, γ
12.7 mm	254 mm	235 mm	0.812 kg m^2	65.2 1/s
Total Turret Mass, M_t	Total Turret Moment of Inertia, I_t	Young's Modulus for 7075-T651 Aluminum alloy, E		Density for 7075-T651 Aluminum alloy, ρ
1.511 kg	6.4 $\cdot 10^{-3}$ kg/m^3	71.7 GPa		2,810 kg/m^3

and

$$\lambda = L\left[\frac{(\omega^2 - i\gamma\omega)m}{E \cdot I_p}\right]^{1/4}$$

In Eq. (4), $G_{steady} = \frac{L^3}{3E \cdot I_p}$ is a steady turret spanwise displacement under steady unit forcing.

To measure the damping coefficient of the aluminum plate, γ, additional measurements were conducted on a separate rectangular aluminum bar of the same thickness. One end of the bar was clamped, and the free end of the beam was deflected and suddenly released. The resulted damping motion of the bar was recorded by a single-axis accelerometer, mounted on the free end of the bar. Analysis of the bar response was conducted and the damping coefficient was measured to be $\gamma = 65.2$ 1/s, see Roeder (2020) for additional details of the experiment and the analysis.

For the presented studies, the turret diameter was chosen to be $D = 0.254$ m and the freestream Mach number to be between $M = 0.3$ and 0.6. For these parameters, $St_D \sim 0.15$ corresponds to a range of frequencies between 80 and 100 Hz, so the target oscillating frequency of the system was chosen to be 90 Hz. The plate material was 7075-T651 aluminum alloy, which was selected for its fatigue-resistant properties. All relevant parameters of the turret and the plate used to compute the resonant frequency are presented in Table 1. To find the relationship between the main resonant frequency of the oscillating turret system as a function of plate length, L, and plate thickness, h, a location of the first resonant peak of $G(\omega)$ was computed for given values of L and h. Fig. 1(b) shows a plot of the predicted main oscillating frequencies for different plate thicknesses and lengths. The red curve describes the desired frequency of 90 Hz. Based on this plot, the thickness of the aluminum plate was chosen to be $h = 12.7$ mm and the plate length was selected to $L = 230$ mm. The plate width was chosen to be $w = 254$ mm. All relevant parameters of the oscillating turret assembly are summarized in Table 1.

Using the parameters in Table 1, the theoretical transfer function, $G(\omega)$, normalized by the steady position, G_{steady}, was numerically calculated and its amplitude and phase are shown in Fig. 2. The first resonant frequency was found to be

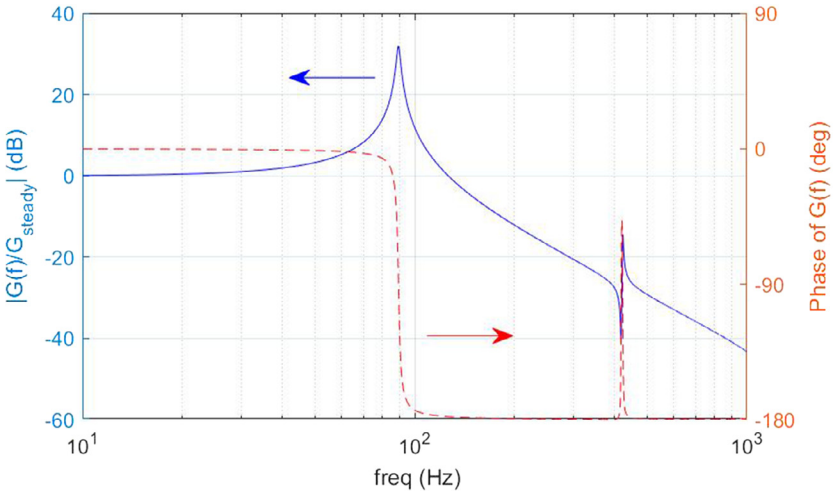

Fig. 2. Amplitude and phase of the theoretical spectral response to the input forcing, Eq. (4) for the parameters in Table 1.

89.4 Hz, where the amplitude reaches 32 dB and the phase drops from zero to −180 degrees. Above this frequency, the amplitude decays at a rate of −40 dB/decade and the phase stays at −180 degrees. The only exception is near the second resonant frequency of 423.3 Hz, where the amplitude has a drop, followed by a secondary peak, while the phase approaches zero before dropping back to −180 degrees. With the exception of this narrow frequency range, it was concluded that the oscillating turret can be modeled as a linear second-order underdamped system with the main resonant frequency of 89.4 Hz.

3. Experimental studies

Based on the theoretical studies, outlined above, the turret assembly was designed and built. A photograph of the oscillating turret assembly and a schematic of the oscillating turret design are presented in Fig. 3. To allow for the turret motion, the bottom of the mounting plate with the hemisphere affixed to it was aligned with the tunnel wall with a small, in the order of a millimeter, gap in between. The oscillating turret assembly was converted to the stationary turret configuration by inserting metal spacers between the mounting disk and the vibrating plate, so the mounting disk was pressed against the tunnel wall. These configurations enabled two different sets of experiments to be made in order for the wake flow physics and dynamic effects of the oscillating turret to be compared to the same, but stationary turret configuration.

Both the oscillating and stationary turret configurations were tested in the University of Notre Dame White Field 3' × 3' wind tunnel facilities at freestream Mach numbers of $M = 0.3$, 0.4, 0.5 and 0.6. The corresponding range of Reynolds numbers was $1.7 \times 10^6 \leq Re_D \leq 2.6 \times 10^6$. A schematic of the experimental setup is presented in Fig. 4. A fast-response Pressure-Sensitive Paint (PSP) was used to collect unsteady pressure fields on and around the turret. A very thin uniform layer, about 60 μm, of PSP was sprayed on the plastic dome and the surrounding aluminum mounting wall section before testing was conducted. The binder material was polymer–ceramic PSP (PC-PSP), which consisted of Silicone RTV as the polymer and bathophen ruthenium as the luminophore. Four 400 nm ultraviolet lights (ISSA LM2-400 type) were used to illuminate the PSP on and around the turret. Two high-speed cameras, Phantom v1611 and Phantom v2512, were used to simultaneously record the fluorescence intensity fluctuations emitted by the PSP. Both cameras were ran at a sampling frequency of $f_{samp} = 3$ kHz at the maximum pixel resolution of 1280 × 800, giving the spatial resolution of 0.54 mm/pixel. The v1611 camera collected 16,541 frames over 5.51 s, and the v2512 camera collected 49,685 frames over 16.56 s. Seven subminiature differential pressure transducers, Type XT-140(M), were used to perform in-situ calibration of the PSP; four pressure transducers were installed on the turret model and three pressure transducers were instrumented on the tunnel wall in the wake region. Independent calibration curves for each pressure transducer were constructed using a pressure chamber before the pressure transducers were installed. The transducers were sampled at 30 kHz for 30 s.

In addition to pressure measurements, a total of eight 1-axis accelerometers, made by PCB Piezotronics, Model 352C33, were affixed to various locations inside of the turret and on the mounting plate and the mounting canister to monitor the turret response. The analysis of the accelerometer data is outside the scope of this paper, and an interested reader is referred to Roeder (2020) for a full discussion of the accelerometer data.

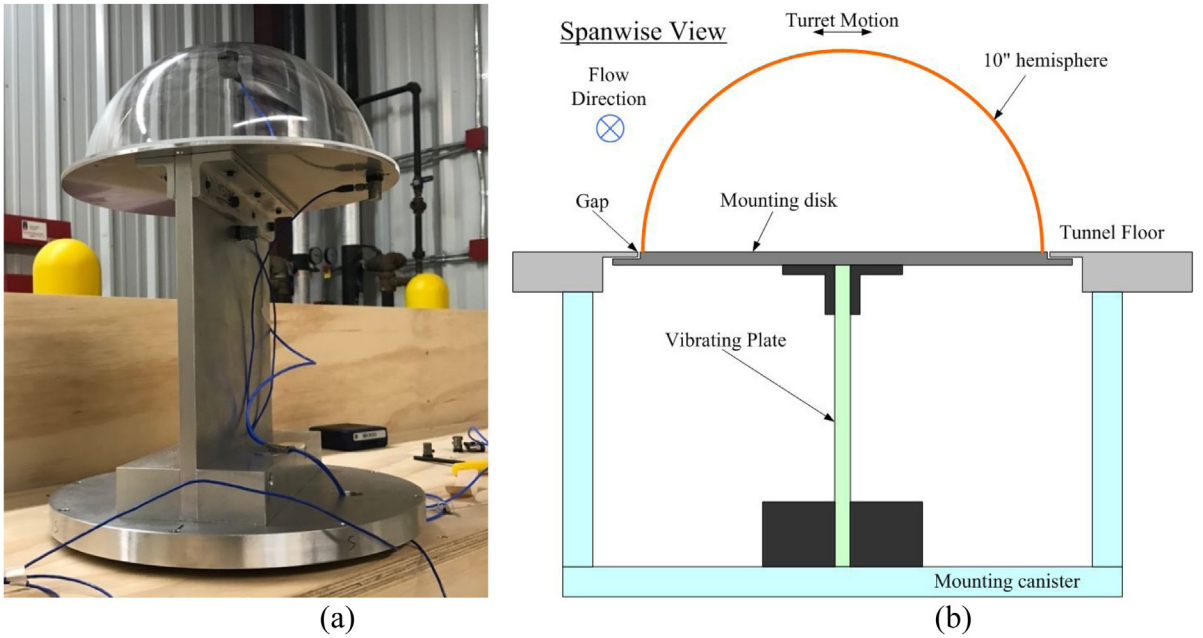

Fig. 3. (a) Photograph of the turret assembly, without a mounting canister. (b) Schematic of the oscillating turret assembly.

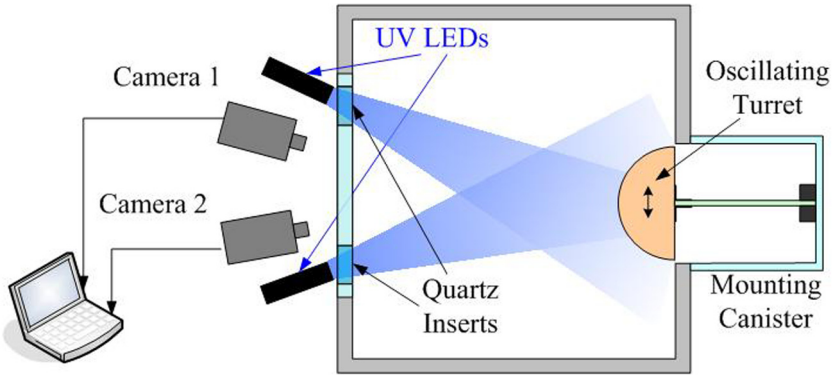

Fig. 4. Schematic of the experimental setup.

4. Data analysis

The instantaneous intensity variations, I, emitted by PSP are related to the instantaneous local static pressure values, P, via the Stern–Volmer equation,

$$\frac{I_{ref}}{I} = A + B\frac{P}{P_{ref}}, \tag{5}$$

where I_{ref} and P_{ref} describe the instantaneous intensity and pressure values, respectively, under a set of reference conditions, and A and B are experimentally determined coefficients. Reference data were collected before each test under no flow conditions with the ultraviolet lights turned on. The spatio-temporal averaged intensity from PSP inside a small annular region immediately surrounding each of the seven pressure sensors were extracted and computed under the reference conditions and at each of the four Mach numbers tested, and the static pressures from the pressure transducer were used in order to determine A and B for each test case. The resulting calibration curve from the in-situ calibration is presented in Fig. 5(a). By computing a linear fit to this curve, the A and B coefficients in Eq. (5) were found to be $A = 0.64$ and $B = 0.33$.

To investigate the frequency response of the PSP, time-resolved spatial-averaged intensities of PSP around the unsteady pressure sensor, located in the middle of the wake, were extracted. After converting the unsteady intensity into the unsteady pressure using Eq. (5), the pressure power spectrum from PSP intensity data was computed and compared

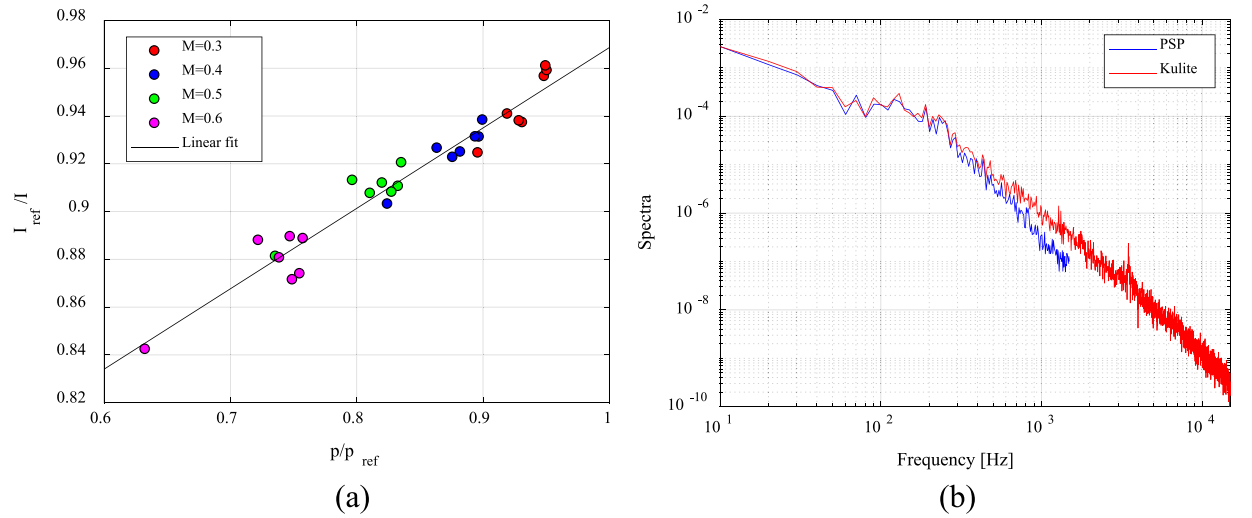

Fig. 5. (a) Calibration curve using in-situ PSP data for freestream Mach numbers $M = 0.3$–0.6. (b) Comparison of normalized PSP pressure spectra for the oscillating turret at $M = 0.5$ with unsteady pressure spectra in the middle of the wake.

to the power spectrum of the unsteady pressure sensor; the result is presented in Fig. 5(b). The agreement between the spectra is reasonable, and the PSP was found to correctly resolve the unsteady pressure spectrum up to approximately 700 Hz. A similar agreement was found using the PSP at the other six pressure transducer locations (not shown), verifying the accuracy of the in-situ calibration. The slight deviations at higher frequencies are likely attributed as a characteristic of the PSP response.

The calibration coefficients in Eq. (5) also depend on the temperature variations (Hayashi and Sakaue, 2020), potentially affecting the accuracy of the pressure measurements. To study this effect, a coupon pained with PSP was placed into a test chamber where both the pressures and the temperatures were varied and A and B coefficients were calculated at different temperatures. Results (not shown) has revealed that both constants increased with the increasing temperature at the rates of approximately 1.2%/°C for the A coefficient and about 1.3%/°C for the B coefficient in the range of 20–25 °C. As the temperature changes during the tunnel runs were measured to be less than 2 °C, the temperature variation of A and B coefficients in Eq. (5) was neglected in these studies.

After extracting the surface pressure fields, the time-averaged fields were computed and removed from the instantaneous pressure fields to produce the fluctuating pressure fields, $p(x,y,z,t)$, for different test cases and Mach numbers. Using these data, the normalized mean-removed coefficients of pressure distributions, C_p, were computed for each Mach number and turret configuration as $C_p(x,y,z,t) = [p(x,y,z,t) - p_\infty]/q_\infty$, where p_∞ and q_∞ denote the freestream static and dynamic pressures, respectively. The spatial distribution of the temporal root-mean-squared coefficients of the fluctuating pressure, $C_{p,rms}(x,y,z) = \sqrt{\overline{C_p{}^2(x,y,z,t)}}$, were calculated in order to study the unsteady pressure distribution in the wake. The overbar here and later in this paper denotes time averaging.

An alternative way to characterize the surface pressure fields in the wake of the turret is to compute an associated surface convective velocity field, $(U(x,z), V(x,z))$, assuming that the surface pressure field is a primarily convecting field,

$$\frac{\partial p(x,z,t)}{\partial t} + U(x,z)\frac{\partial p(x,z,t)}{\partial x} + V(x,z)\frac{\partial p(x,z,t)}{\partial z} = 0. \tag{6}$$

This equation is commonly known as the optical flow equation. One way to solve it to use the Lucas–Kanade method (Lucas and Kanade, 1981). If the pressure field is given at several consecutive time points, Eq. (6) at every spatial point can be treated as an overdetermined system of equations for the two velocity components at this spatial point (Lucas and Kanade, 1981; Lee et al., 2018, 2020). It can be solved using the least-squares minimization technique, resulting in the following equations for the velocity components,

$$\begin{aligned} U(x,z) &= \frac{\sum_t \frac{\partial p}{\partial t}\frac{\partial p}{\partial x}\sum_t \left(\frac{\partial p}{\partial z}\right)^2 + \sum_t \frac{\partial p}{\partial t}\frac{\partial p}{\partial z}\sum_t \frac{\partial p}{\partial x}\frac{\partial p}{\partial z}}{\left(\sum_t \frac{\partial p}{\partial x}\frac{\partial p}{\partial z}\right)^2 - \sum_t \left(\frac{\partial p}{\partial x}\right)^2 \sum_t \left(\frac{\partial p}{\partial z}\right)^2} \\ V(x,z) &= \frac{\sum_t \frac{\partial p}{\partial t}\frac{\partial p}{\partial z}\sum_t \left(\frac{\partial p}{\partial x}\right)^2 + \sum_t \frac{\partial p}{\partial t}\frac{\partial p}{\partial x}\sum_t \frac{\partial p}{\partial x}\frac{\partial p}{\partial z}}{\left(\sum_t \frac{\partial p}{\partial x}\frac{\partial p}{\partial z}\right)^2 - \sum_t \left(\frac{\partial p}{\partial x}\right)^2 \sum_t \left(\frac{\partial p}{\partial z}\right)^2} \end{aligned} \tag{7}$$

This approach was proposed in Lee et al. (2018, 2020) to compute the global skin friction fields, using luminescent oil-film images. An alternative way to solve Eq. (6) is to use the Horn–Schunck method, as described in Liu et al. (2008) and Liu and

Shen (2008), but it requires computing second-order partial derivatives of the pressure field and thus it is more sensitive to measurement noise. Eq. (7) uses only the first-order partial derivatives, which are less sensitive to the noise. In addition, if many time instances are used, the system of equations, Eq. (7), is an over-determined system and, as a result, the error in computing the velocity components is further reduced. All derivatives in Eq. (7) were numerically estimated from the surface pressure field using a first-order discrete approximation

Proper Orthogonal Decomposition (POD) is commonly used as a means for creating a low-order reconstruction of the spatio-temporal data, where the data can be adequately represented using a reduced number of spatial modes (Taira et al., 2017). In POD, the globally-reconstructed spatio-temporal signal, $p(s, t)$, where $s = (x, y, z)$ denotes a spatial point, is decomposed into a series of orthonormal spatial POD modes, $\varphi(s)$, and corresponding temporal coefficients, $a_n(t)$, such as $p(s,t) = \sum_n a_n(t)\varphi_n(s)$. The energy of each mode is $\lambda_n = \overline{a_n^2(t)}$.

Although an optimal set of modes can be obtained for each data set using POD, the spatial modes are different for each case, so comparing POD modes and related energies for different cases becomes complicated. An alternative way, called Joint Proper Orthogonal Decomposition (JPOD), was proposed as a data analysis technique to compute the common or joint modes from different data sets (Gordeyev et al., 2014). JPOD is a specialized version of POD, in which the spatio-temporal data for different cases are combined into a single joint data set, and POD algorithm is used to extract the joint spatial modes. By design, this set of spatial JPOD modes is the same to all cases. When the individual data sets for each case are projected onto these spatial JPOD modes, the temporal coefficients and the corresponding energies will be different. Thus, the differences among cases will be reflected in the temporal coefficients and the energy distributions.

In the present studies, the pressure fields in the wake region for the oscillating and the stationary turret configurations were combined to compute spatial JPOD modes. The temporal coefficients of JPOD modes were also computed and their power spectra were analyzed. From the temporal coefficients, individual energies of JPOD modes were computed.

By integrating the unsteady fluctuating pressure field over the hemispherical turret surface, the unsteady fluctuating forces acting on the turret, $\overrightarrow{F}(t) = \{F_x(t), F_y(t), F_z(t)\}$, were computed. All three components of the force were normalized by the dynamic pressure and the cross-sectional area of the turret, $S_{cross} = 0.5\pi(D/2)^2$, yielding a non-dimensional time-dependent force coefficients, $\{C_x(t), C_y(t), C_z(t)\}$. Using these force coefficients, temporal root-mean-squared values and the power spectra were calculated for each force component.

The temporal spanwise displacement of the turret in the oscillating case was measured directly by optically tracing the motion of the turret edge. This was accomplished by extracting a single 1×10 column of pixels (0.54 mm $\times$ 5.4 mm) spanning the gap region and tracking the relative position of the intensity threshold corresponding to the turret edge. The exact position of the turret edge was resolved for each frame by interpolating the intensity values of adjacent pixels in order to achieve displacement resolution within the subpixel range. The edge position of the oscillating turret, z_{turret}, was computed for the entire time series at all three tested Mach numbers.

Finally, in order to study the intermittency of the applied forcing and the turret motion during the stationary and the oscillating cases, a conditional analysis using a Morlet wavelet analysis (Gordeyev and Thomas, 1999) was used. The wavelet transformation of a continuous signal, $g(t)$, is generally defined as,

$$G_\Psi(\kappa, \tau) = \kappa \int_{-\infty}^{\infty} g(t)\Psi^*(\kappa(t-\tau))dt \tag{8}$$

where $\Psi(\eta)$ is the wavelet mother function, κ is a dilatation parameter, τ is a translation or shift parameter and an asterisk denotes a complex conjugate. Morlet mother function is defined as $\Psi(\eta) = \exp\left(id\eta - \frac{\eta^2}{2}\right) - \exp\left(\frac{d^2}{2} - \frac{\eta^2}{2}\right)$, where $d = 6$ was chosen for this study. The Morlet wavelet transform is useful to study temporal amplitude variation of the signal at a given frequency. The frequency is related to the dilatation parameter as $f(\kappa) = (d\kappa)/(2\pi) \approx 0.96\kappa$. The local amplitude of the Morlet wavelet transform was computed as $A_\Psi(\tau; f) = |\, G_\Psi(f(\kappa), \tau)|$.

5. Experimental results

5.1. Oscillating turret motion

Time series of the turret position in the spanwise direction for the oscillating case were extracted, as discussed before, and auto-correlation spectral densities at $M = 0.4$, 0.5 and 0.6 are presented in Fig. 6. The spectra for the oscillating turret reveals the presence of a single strong peak at a frequency of 87 Hz. This value is close to the theoretical main resonant frequency of 89.4 Hz, predicted by the oscillating turret model. In addition to the dominant peak, the first and the second harmonics at 174 Hz and 260 Hz, respectively, with much smaller levels of spectral energy are also present in the spectra, indicating a small degree of non-linear effects in the turret response. A range of low frequencies, centered around 15 Hz, are also present in the spectra, and, as it will be shown later in this paper, they are related to the intermittent nature of the turret motion.

The time series of the extracted turret position for the oscillating case at $M = 0.5$ are presented in Fig. 7 as a thin blue line. The time series show intermittent bursts up to 0.5 mm in amplitude with durations of few hundred of D/U_∞. Note that the turret motion relative to the turret diameter is small, $|\, z_{\text{turret}}|/D < 2\%$. The amplitude of Morlet wavelet transform of the edge motion was extracted at the 87 Hz main resonant frequency and is presented in Fig. 7 as a thick

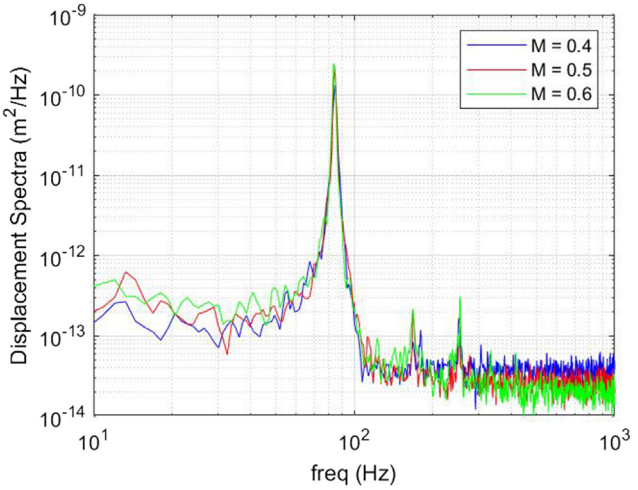

Fig. 6. Auto-correlation spectral densities of turret spanwise displacement for the oscillating case at $M = 0.4$, 0.5 and 0.6.

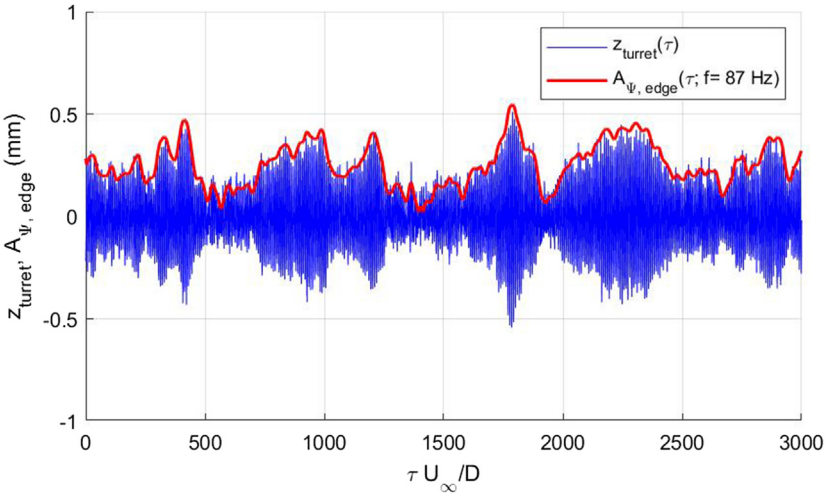

Fig. 7. Time series of the turret spanwise motion, z_{turret}, (thin red line) and amplitude of Morlet wavelet transform at the main resonant frequency, $A_\psi(\tau; f = 87$ Hz) (thick red line) for the oscillating case at $M = 0.5$. (For interpretation of the references to color in this figure legend, the reader is referred to the web version of this article.)

red line, outlining the bursts in the turret position. Similar intermittency of the turret spanwise motion were observed at other test Mach numbers. As the source of the turret oscillations is the spanwise unsteady forcing, this behavior confirms the intermittent nature of the unsteady spanwise forcing, acting on the turret. We will provide additional analysis of the intermittent forcing later in this paper.

5.2. Unsteady pressure fields

The spatial distribution of $C_{p,rms}(x, z)$ for the oscillating and stationary turret cases at $M = 0.4$, 0.5, and 0.6 are presented in Fig. 8. The unsteady pressure fields for both cases are approximately symmetric in the spanwise direction, indicating a symmetric wake. The unsteady neckless vortex, formed in front of the turret, is responsible for the increase in $C_{\text{p,rms}}$ in this region. The unsteady separation over the turret results in the increase in the pressure fluctuations, visible as a narrow region aligned in the spanwise direction on top of the turret. Finally, an inherently unsteady re-attachment line downstream of the turret creates a crescent-shaped region of large pressure fluctuations downstream of x/R = 1.35. Overall, the spatial map of the fluctuating pressure is very similar to ones previously observed in other studies of the pressure fields on and around hemispheres at subsonic speeds (De Lucca et al., 2018a,b; Gordeyev et al., 2018).

Before continuing, a comment should be made about the effect of the oscillating turret motion on the accuracy of the PSP measurements. As can be seen in Fig. 7, the maximum amount of the turret motion in the spanwise direction is

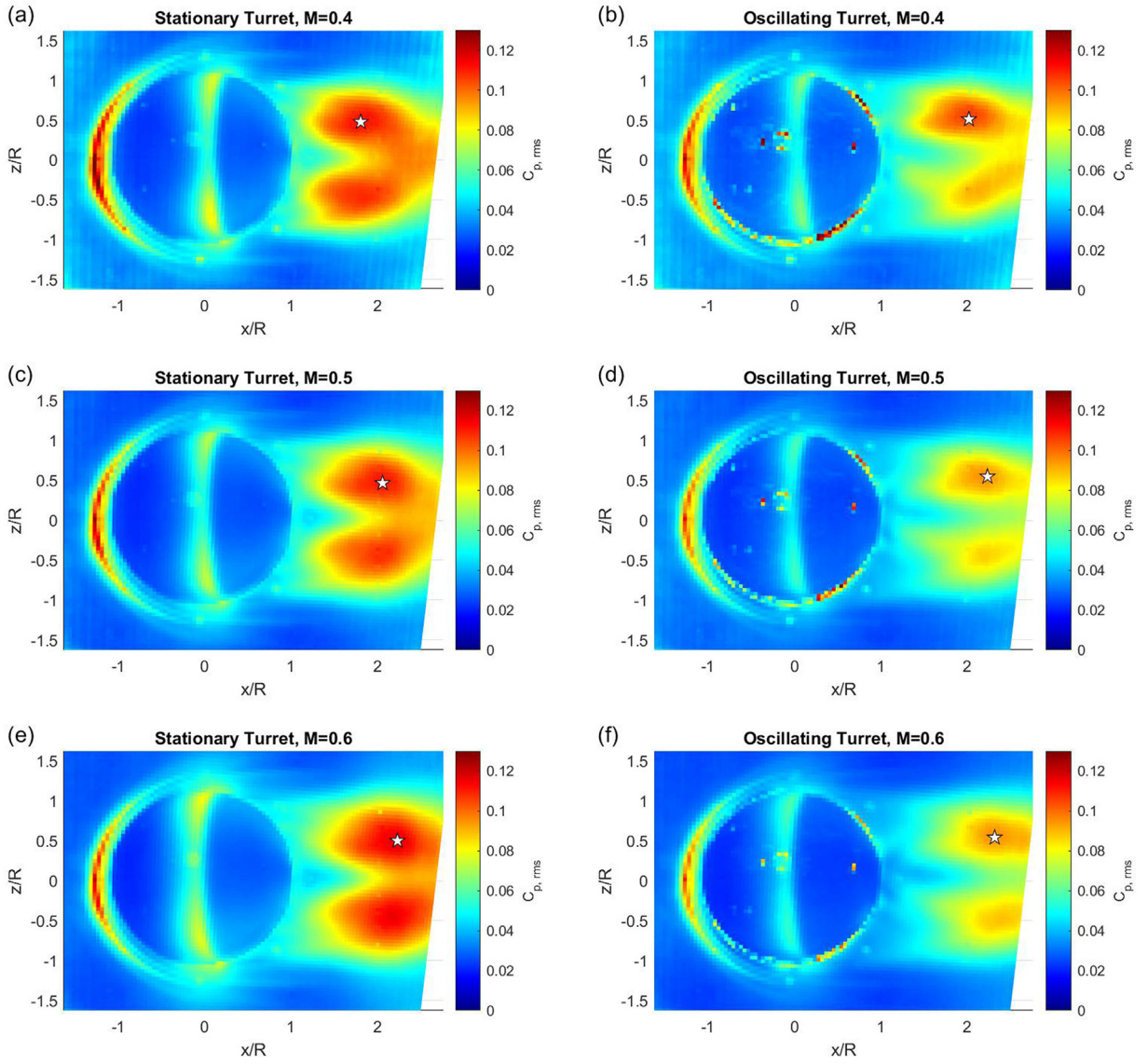

Fig. 8. Spatial distributions of $C_{p,rms}(x, z)$ for (a,c,e) the stationary turret case and for (b, d, f) the oscillating turret case for (a, (b) $M = 0.4$, (c, (d) $M = 0.5$ and (e, (f) $M = 0.6$. The locations of the maximum $C_{p,rms}$ in the wake are indicated by a star.

± 0.5 mm, or approximately one pixel. Since the images of the turret and the wake region do not have any sharp spatial variations, this uncertainty in the spatial position does not create any discernable errors in computing the pressure fields. The only place this motion has an effect on the reconstructed pressure fields is the region at the turret edge, where the images have a sharp gradient along the turret edge, between the turret and the tunnel wall. This sharp intensity variation will result in unphysical values of the pressure field in this region. It can be seen in Fig. 8(b, d, f) as a sharp, but very localized increase in $C_{p,rms}$ along the turret edge. To remove this contamination, this region was masked out from the pressure data.

For the oscillating turret, the source of the turret motion is the unsteady force acting on the turret. As it requires energy to move the turret, the overall turbulent energy in the wake should decrease. Indeed, as it can be seen in Fig. 8, there is a noticeable difference between the pressure fields for the oscillating and stationary cases, as the oscillating turret does weaken the turbulent wake, as well as increases its streamwise extent. To demonstrate this extent of the unsteady pressure region, the locations of the maxima of the fluctuating pressure field in the wake for both cases at different Mach numbers are indicated by star symbols in Fig. 8; the streamwise locations of the maxima in $C_{\mathrm{p,rms}}$ are also presented in Table 2. The location of the maximum pressure variation in the wake moves farther downstream from the turret with

Table 2
Streamwise locations of the maxima of $C_{p,rms}$ in the wake of the turret for different cases and Mach numbers.

M	0.4	0.5	0.6
x_{max}/R, Stationary Turret	1.81	2.06	2.23
x_{max}/R, Oscillating Turret	2.02	2.24	2.32

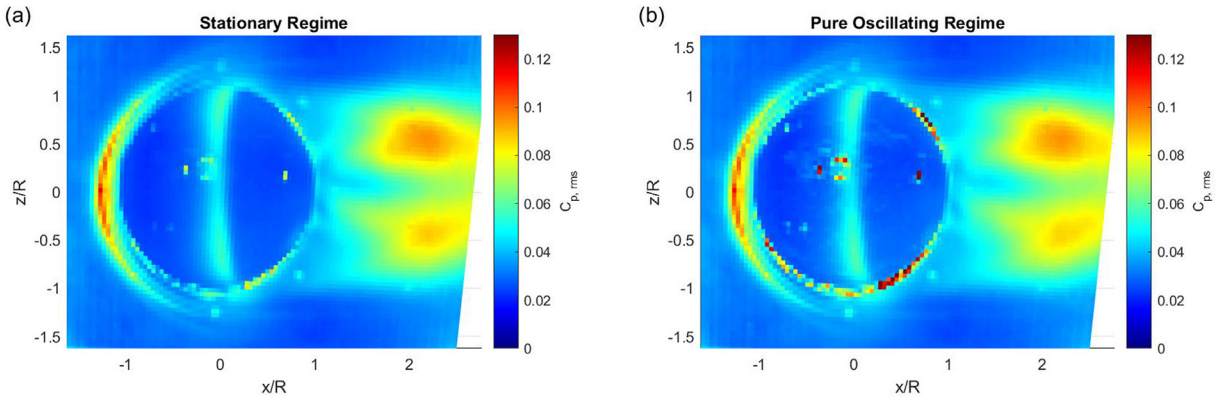

Fig. 9. Conditionally-averaged $C_{p,rms}(x, z)$ during (a) the mostly stationary state and (b) the strong oscillating regime for the oscillating turret case at $M = 0.5$.

the increased Mach number and these locations are shifted even farther downstream for the oscillating case, compared to the stationary case, for all measured Mach numbers.

A threshold of 0.3 mm, corresponding to the time-averaged value of the wavelet amplitude of the edge motion in Fig. 7, was used to identify time intervals where the turret exhibits a strong oscillatory behavior and when it is mostly stationary. Using this threshold, unsteady pressure fields for the oscillating case during time intervals above the threshold were separated into a strong oscillating regime, and the pressure fields during time intervals below the threshold were separated into the mostly stationary state. The corresponding conditionally-averaged spatial maps of $C_{p,rms}$ were computed and are presented in Fig. 9 for $M = 0.5$. There is a very little change in the wake response during the mostly stationary and the strong oscillating regimes. The threshold value was varied between 0.1 and 0.4 mm and the resulting spatial pressure maps were found to be nearly independent of the amplitude threshold. Similar results were observed for other measured Mach numbers and therefore are not shown here. This behavior indicates that the wake pressure field for the oscillating turret does not respond quickly enough to intermittent changes in turret motion. In other words, when the oscillating turret becomes primarily stationary during short intervals of time, for instance, between $500 \leq tD/U_\infty \leq 750$ in Fig. 7, the statistics of the wake pressure field do not appear to respond to these changes.

As it was mentioned in the Introduction, the dominant frequency range of the anti-symmetric wake motion is $St_D = f_{peak}D/U_\infty = 0.1$–$0.2$, which corresponds to a typical time scale of $T_{wake} = 1/f_{peak} = 5$–$10\ D/U_\infty$. Thus, the durations of the strong turret oscillations of 100–200 D/U_∞, observed in Fig. 7, would correspond to 10–40 T_{wake}. No visible changes in the conditionally-averaged pressure fields during the primarily stationary and the strong oscillating regimes, shown in Fig. 9, indicates that the wake downstream of the turret needs longer than ∼20 wake time scales to adjust to a changing environment.

5.2.1. Convective velocity fields

To quantify the surface topology of the wake, unsteady pressure fields were used to compute the convective velocities, $(U(x, z), V(x, z))$, in the wake of the turret, using Eq. (7). Resultant U- and V- fields for the stationary case at $M = 0.5$ are presented in Fig. 10(a, b). The U-component is spanwise symmetric and positive in two regions: in front of the turret and downstream of it. The first region is associated with the footprint of the necklace vortex in the front of the turret, while the second region indicates vortical turbulent structures, formed in the turbulent wake and convecting downstream. The streamwise velocity of these wake structures reaches $0.14U_\infty$ at $x/R = 2$; similar velocity magnitudes of $\sim 0.2U_\infty$ were reported in McCarthy et al. (2019). The recirculating region immediately adjacent to aft of the turret is characterized by the negative streamwise velocity, indicated as a blue region in Fig. 10(a). The location of the saddle point, indicative of the streamwise size of the recirculating region, and defined as a zero-crossing of the streamwise velocity along the centerline $y = 0$, is denoted as an open circle in Fig. 10(a, c).

The spanwise V-velocity, shown in Fig. 10(b), is anti-symmetric in the z-direction and essentially non-zero in the same regions, where the U-component is positive. At both sides of the wake region, the V-velocity changes a sign, indicating a divergent flow in the spanwise direction and marking the boundary of the recirculating region. This region is clearly

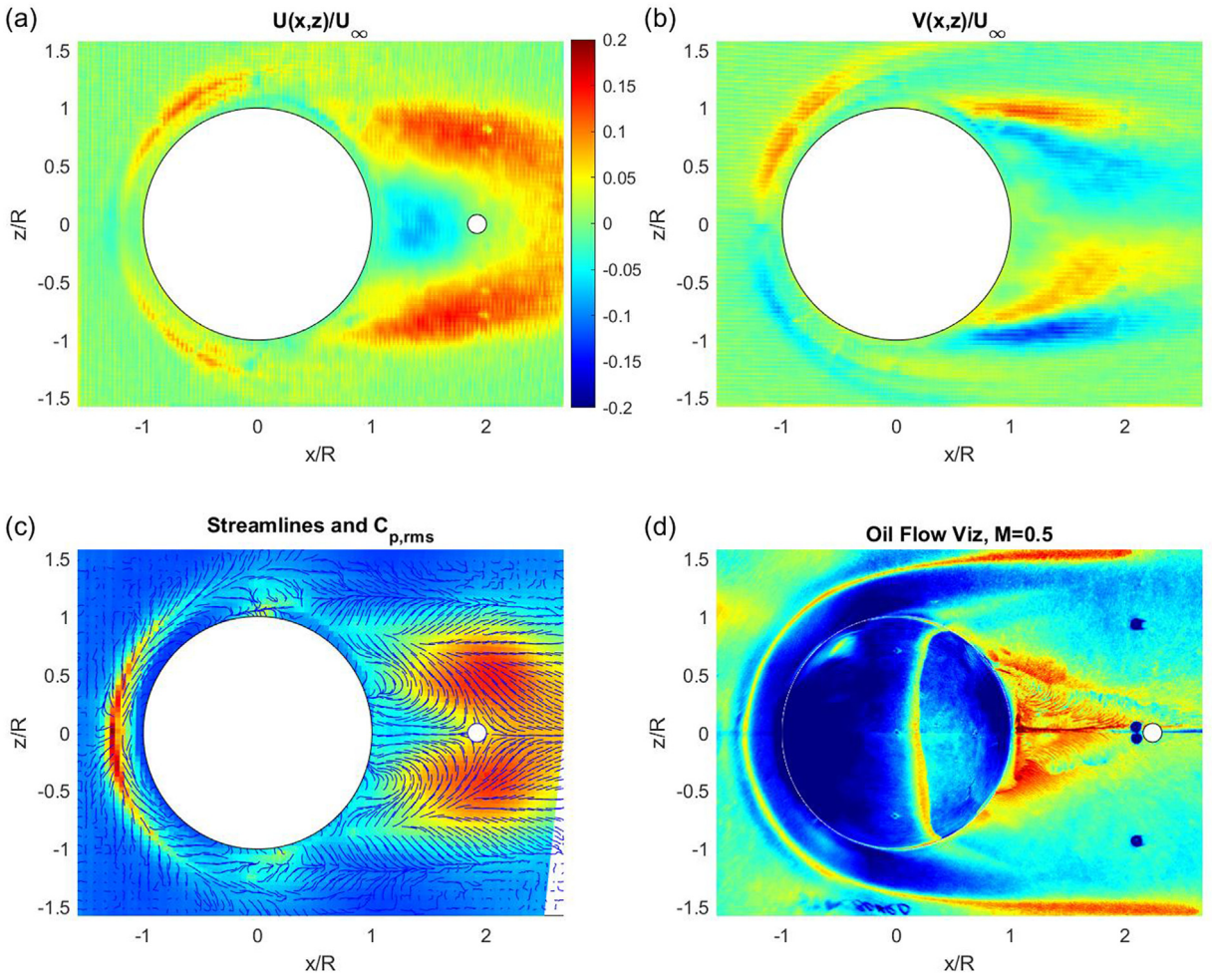

Fig. 10. Normalized convective (a) streamwise velocity, (b) spanwise velocity and (c) streamlines with superimposed $C_{p,rms}$ field from Fig. 8(c), for the stationary turret at $M = 0.5$. (d) Oil flow visualization of the wake topology around the hemisphere at $M = 0.5$, adapted from Gordeyev et al. (2016). Locations of the saddle points along the re-attachment line are indicated by open circles in (a, c, d).. (For interpretation of the references to color in this figure legend, the reader is referred to the web version of this article.)

observed in the streamline pattern downstream of the turret in Fig. 10(c). The spatial distribution of the fluctuating field, $C_{p,rms}$ from Fig. 8(c) is also plotted along with the streamline pattern. One region of the increased pressure fluctuations is associated with the unsteady necklace vortex upstream of the turret. Other regions are located along and downstream of the boundary of the recirculating region, associated with the unsteady re-attachment line. Interestingly, the pressure fluctuations are relatively small inside the recirculating region itself. Finally, small increases in the fluctuating pressure are located on both sides of the turret near the flow separation at $x/R = 0$ and are related to vortical structures, observed in Gordeyev et al. (2016) to form at the hemisphere-floor junction. Similar velocity fields were observed at other tested Mach numbers.

Detailed studies of the surface flow topology around a fixed hemisphere using oil flow visualization was conducted by Gordeyev et al. (2016) and the example of the surface oil streak pattern for $M = 0.5$ is presented in Fig. 10(d). Clearly, the streak pattern is very similar to the streamline pattern for the stationary case in Fig. 10(c), computed using the unsteady pressure fields. The location of the necklace vortex in front of the turret is properly measured by both techniques. The location of the saddle point, found to be at 2.2R downstream of the turret and indicated by an open circle in Fig. 10(d), is close to the location of 1.92R, found using the convective velocity field. Also, vortical structures inside the recirculating region at $(x/R, z/R) = (1.2, \pm 0.5)$ can be seen in both patterns. Thus, spatio-temporarily resolved surface pressure fields can also be used to extract and to study the topology of the surface flow around the turret and other geometries.

To study the changes in the surface topology due to the oscillating turret, streamline patterns for both the stationary and the oscillating cases at different Mach numbers are presented in Fig. 11. Since the streamline patterns were found to be spanwise symmetric, only a half of the pattern is plotted in each subfigure. The locations of the saddle points for the stationary and the oscillating cases are indicated by open circles and filled squares, respectively. For the stationary case,

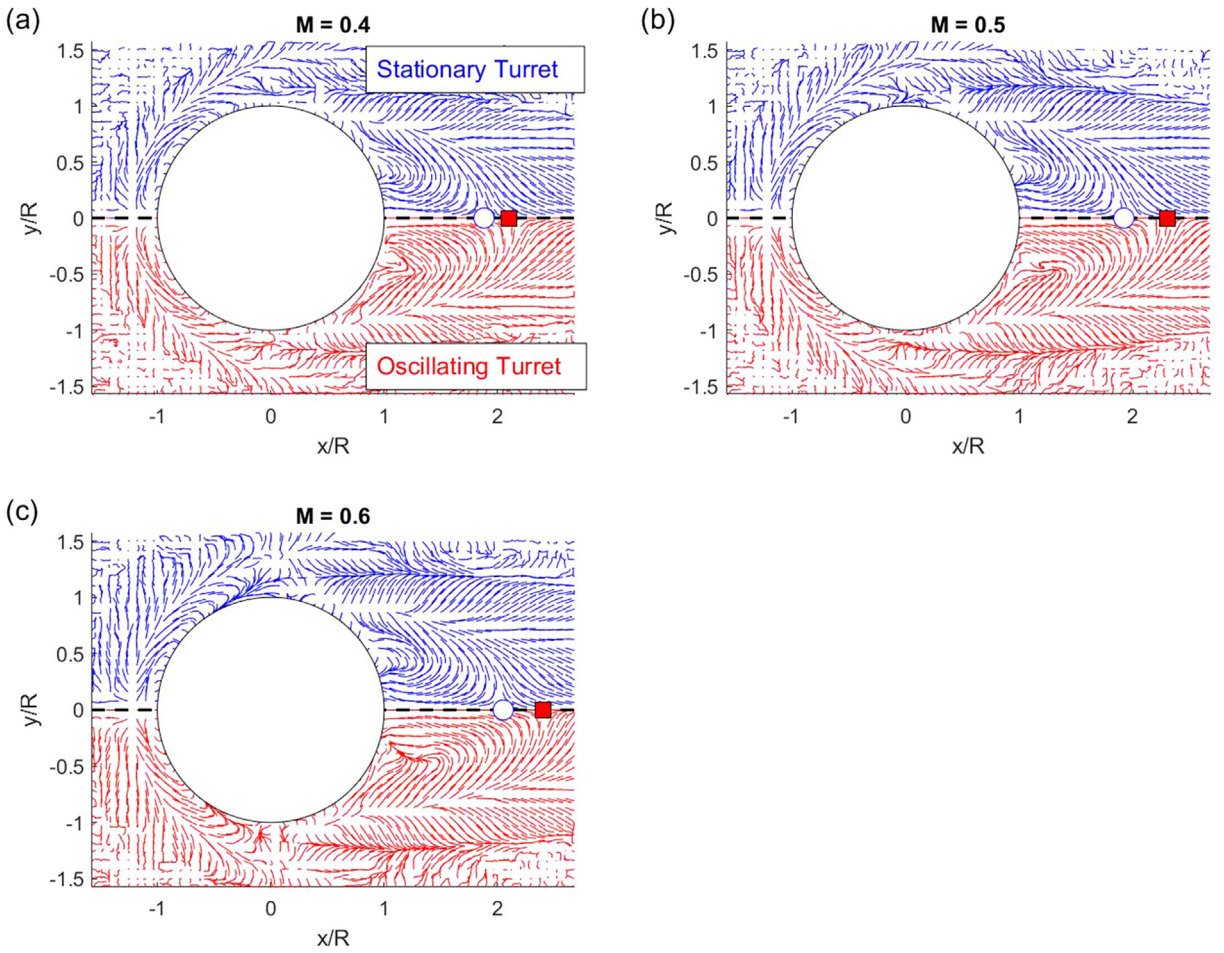

Fig. 11. Streamline patterns for the stationary (upper half in blue) and the oscillating (lower half in red) cases at M = (a) 0.4, (b) 0.5 and (c) 0.6. The locations of the saddle points for the stationary and the oscillating cases are indicated by open circles and filled squares, respectively.. (For interpretation of the references to color in this figure legend, the reader is referred to the web version of this article.)

the location of the saddle point moves farther downstream with increasing Mach number, from $x/R = 1.88$ at $M = 0.4$ to $x/R = 2.05$ at $M = 0.6$. A similar increase in size of the recirculating region was observed using oil-flow visualization in Gordeyev et al. (2016). The trend is also consistent with the downstream shift of the location of the maximum $C_{p,rms}$, shown in Fig. 8. For the oscillating case, the saddle point is always farther away from the turret, compared to the stationary turret case. The largest shift was observed at $M = 0.5$, where the saddle point moves from $x/R = 1.92$ to $x/R = 2.3$. Again, the results are consistent with the similar trends in the location of the maximum $C_{p,rms}$, shown in Fig. 8.

5.3. JPOD analysis of unsteady pressure fields in the wake

The pressure data in the wake of the turret for the stationary and the oscillating cases for $M = 0.5$ were used to perform JPOD analysis. The first six JPOD spatial modes are presented in Fig. 12. The first dominant mode, as well as the third and the fifth modes are mostly symmetric in the spanwise direction, while modes # 2, # 4 and #6 are primarily anti-symmetric in the spanwise direction. The small asymmetry, observed in higher-order JPOD modes # 5 and # 6, can come from several sources, like a small asymmetry in the turret shape and other geometric asymmetries in the experimental set-up, which would lead to a small asymmetry in the wake downstream of the turret. This small asymmetry typically is present in less energetic, higher-order modes. This small asymmetry will be ignored for the rest of the paper, and the modes will be addressed as either symmetric or anti-symmetric ones. In previous studies of the unsteady pressure fields in the wake around hemispherical turrets (De Lucca, 2015; De Lucca et al., 2018b; Gordeyev et al., 2018), the spanwise symmetric modes were associated with the global symmetric separation over the turret, while the spanwise-anti-symmetric modes were attributed to the anti-symmetric vortex shedding.

The relative individual and cumulative energies of the first 100 JPOD modes for the oscillating and stationary cases at $M = 0.5$, normalized by the total energy for the stationary case, are presented in Fig. 13. The first JPOD mode contains

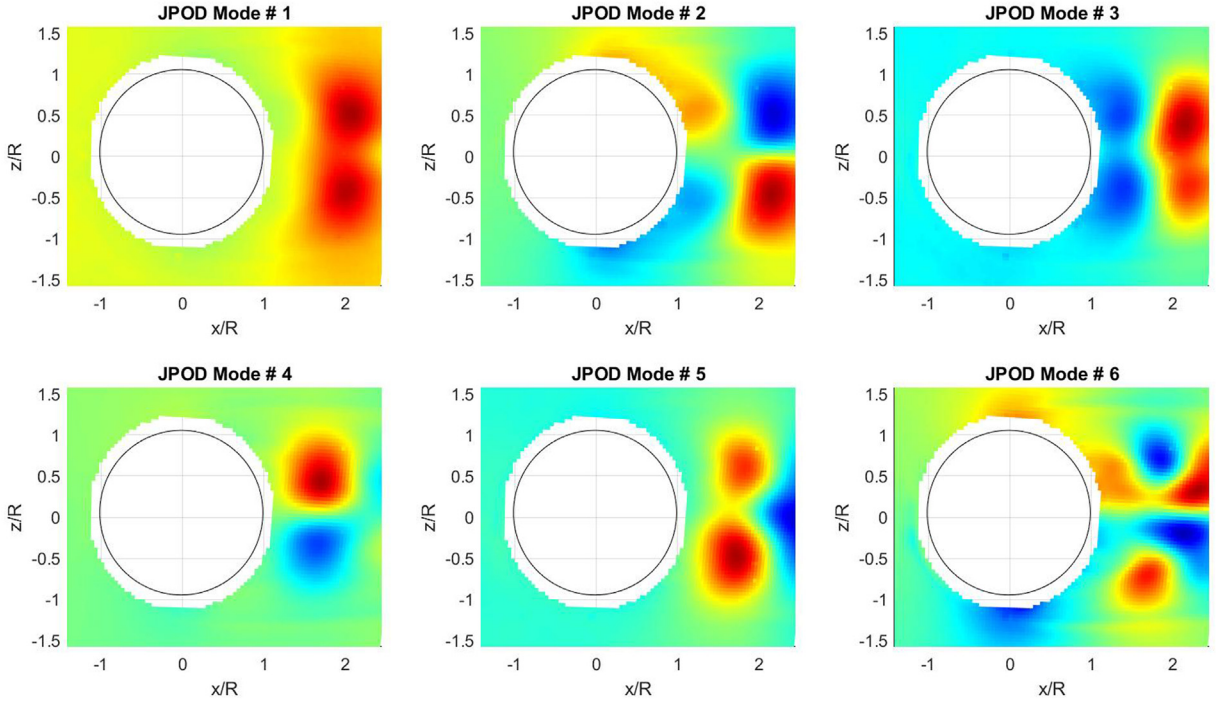

Fig. 12. First six dominant JPOD spatial modes for $M = 0.5$. The turret outline is denoted by a black circle.

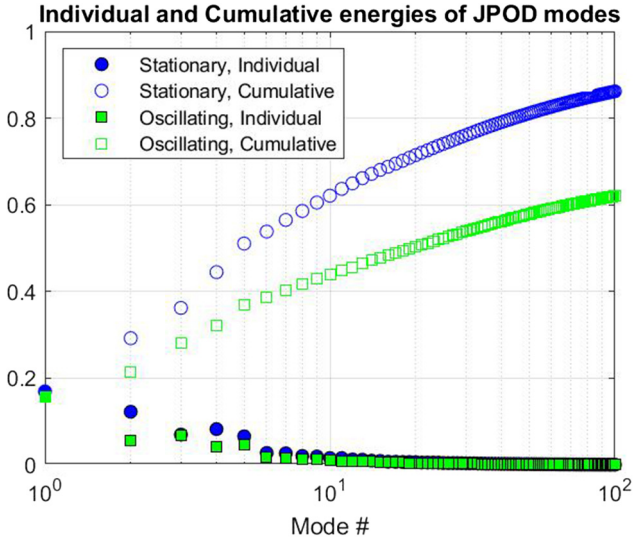

Fig. 13. JPOD cumulative and individual energies, for the oscillating and stationary cases at $M = 0.5$, normalized by the total energy for the stationary case.

about 20% of the total energy for both the stationary and the oscillating cases, and the first six modes contribute about a half of the unsteady pressure energy in the wake region. The cumulative energies for the oscillating case are lower than the cumulative energies for the stationary case, consistent with the smaller $C_{p,rms}$ values in the wake observed in Fig. 8. Further comparing the mode energies of the stationary and the oscillating cases, energies of anti-symmetric modes # 2 and # 4 are significantly reduced by a factor of two, indicating the oscillating turret primarily suppresses the global anti-symmetric shedding.

The spectra of the temporal coefficients, normalized by the square of the dynamic pressure, for the stationary turret case at $M = 0.4$, 0.5 and 0.6 are presented in Fig. 14. All modal spectra collapse over the range of the measured Mach numbers, demonstrating a self-similar behavior of the wake. The spanwise-symmetric modes # 1, # 3, and #5 have most

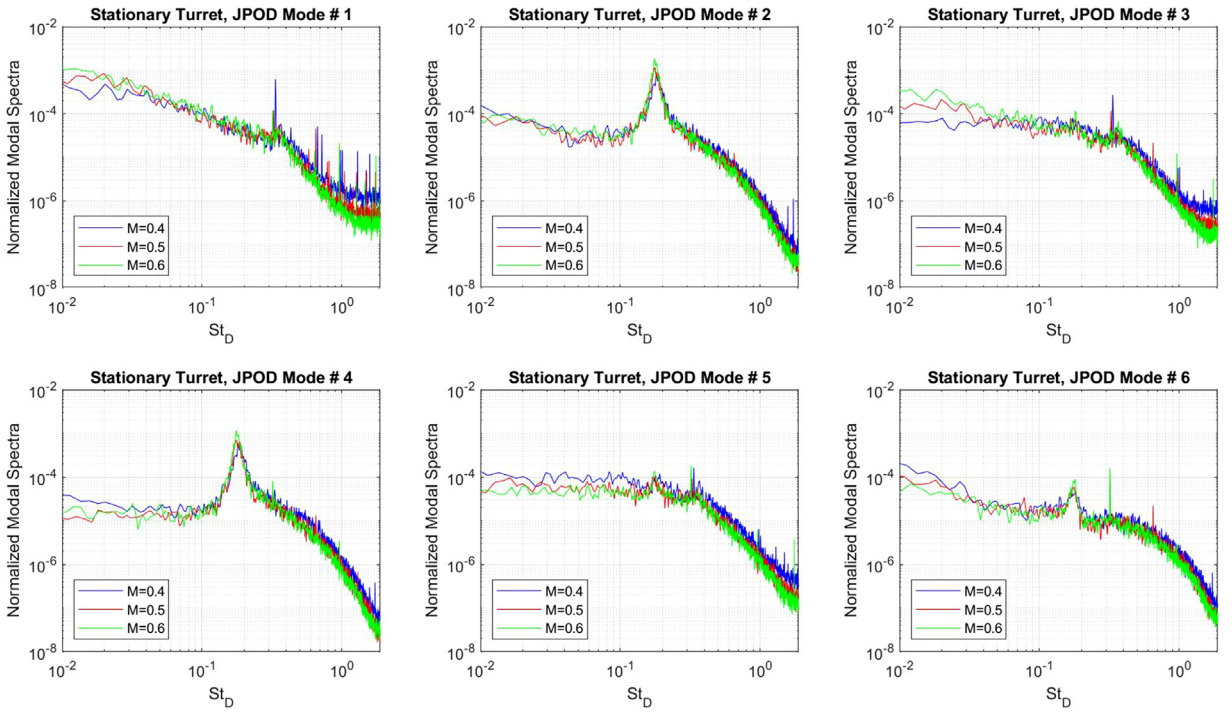

Fig. 14. JPOD temporal coefficient normalized spectra corresponding to the first six dominant JPOD modes for the stationary turret case at $M = 0.4$, 0.5 and 0.6.

of their energy contained in low frequencies. Modes #1 and #3 also exhibit a relative small peak in their spectra around $St_D = 0.35$. This peak is inside the range of $St_D = 0.2$–0.5, associated with the symmetric vortex shedding reported in Manhart (1998). The anti-symmetric motion, represented by JPOD modes #2, # 4 and #6, have distinct peaks in their spectra at approximately $St_D = 0.17$, and this peak is independent of the Mach number. This peak was also observed in previous studies by Gordeyev et al. (2014) and De Lucca et al. (2018b) and also was found to be approximately constant for a range of Mach numbers between 0.35 and 0.66. As discussed in Manhart (1998) and McCarthy et al. (2019), this peak is associated with the anti-symmetric vortex shedding.

A comparison between spectra of the temporal coefficients for the stationary and oscillating cases at $M = 0.5$ is presented in Fig. 15. The normalized spectra of the spanwise symmetric mode, Mode #1, as well as other symmetric modes # 3 and #5, are largely unchanged between the stationary and the oscillating cases. In contrast, the peaks in the spectra of the anti-symmetric motion, represented by JPOD modes #2, #4 and #6, are significantly suppressed for the oscillating case, compared to the stationary case. In addition, the peaks in the spectra of these anti-symmetric modes are shifted toward the main oscillating turret frequency of 87 Hz, indicated as vertical dashed lines in Fig. 15. A very similar peak suppression was observed for $M = 0.4$ and 0.6 and therefore is not shown. This behavior provides a strong evidence that the resulting mechanical motion of the turret driven by the unsteady turbulent flow reduces the overall energy of the global anti-symmetric shedding, while keeping the dynamics of the global symmetric wake motion mostly unchanged.

As discussed in Wood et al. (2018), the consistent reduction in wake pressure energy is logical from an energy conservation standpoint. When the total energy of the flow, which remains constant throughout the control volume of the test section, is partially converted into work being done in order to move the turret back and forth in the spanwise direction, less energy is available in the turbulent wake to form convective structures and to create anti-symmetric and symmetric motion behavior that is readily observed for the stationary turret. This analysis provides useful information that will aid in developing a comprehensive understanding of the flow downstream of a hemispherical spanwise-oscillating turret.

5.4. Analysis of unsteady forces acting on turret

The computed normalized coefficients of unsteady force components are presented in Fig. 16 for the oscillating and stationary cases at $M = 0.4$, 0.5, and 0.6. The highest magnitude of the fluctuating force on the turret occurs in the spanwise z-direction for both cases. The coefficient of force is over 50% higher in the z-direction than in the wall-normal y-direction and between three and four times higher than the streamwise x-direction for both turret configurations at all three Mach numbers. The computed force coefficients for the stationary turret agree reasonably well with the values,

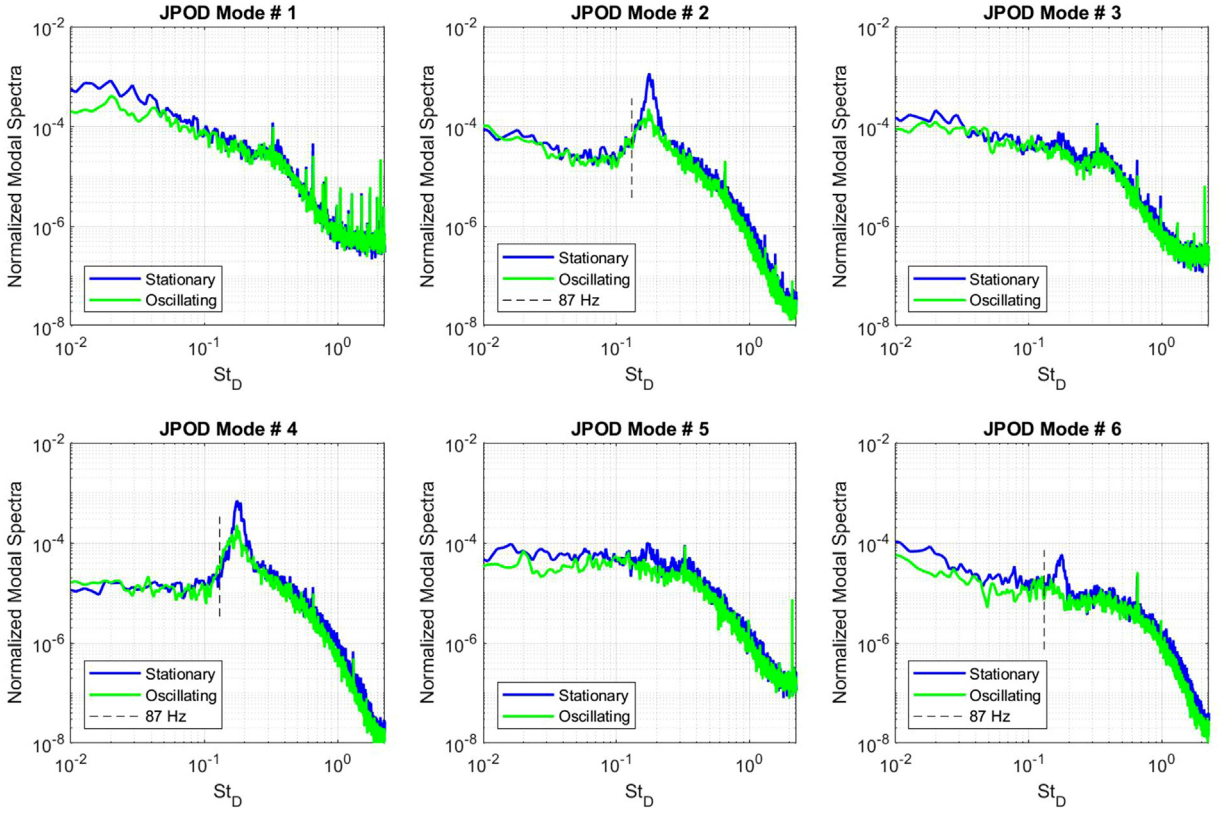

Fig. 15. JPOD temporal coefficient normalized spectra corresponding to the first six dominant JPOD modes for the stationary and the oscillating turret cases at $M = 0.5$. The main oscillating frequency of 87 Hz is indicated as a vertical dashed line.

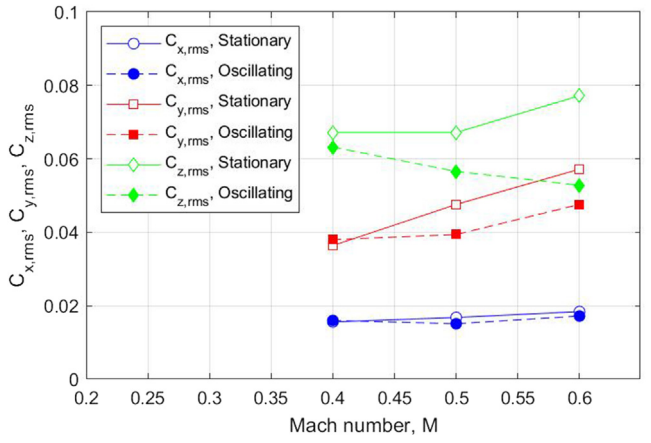

Fig. 16. The coefficients of different force components for various Mach numbers and both the stationary (open symbols) and the oscillating (filled symbols) turrets.

obtained on a slightly different turret geometry, namely on a hemisphere-on-cylinder turret at $M = 0.5$ in De Lucca et al. (2013b), De Lucca (2015).

Generally, the coefficients either weakly increase or stay approximately constant with the increasing Mach number. The drag-related x-coefficients are virtually unchanged by the oscillating turret. The force coefficients for the oscillating case are smaller than the coefficients for the stationary case for z-coefficients and, in lesser degree, for y-coefficients. One way to explain these trends is to recall that the oscillating turret responds to the unsteady pressure acting on it. Let us say the pressure is higher on one side compared to the opposite site. The oscillating turret will start moving in the spanwise

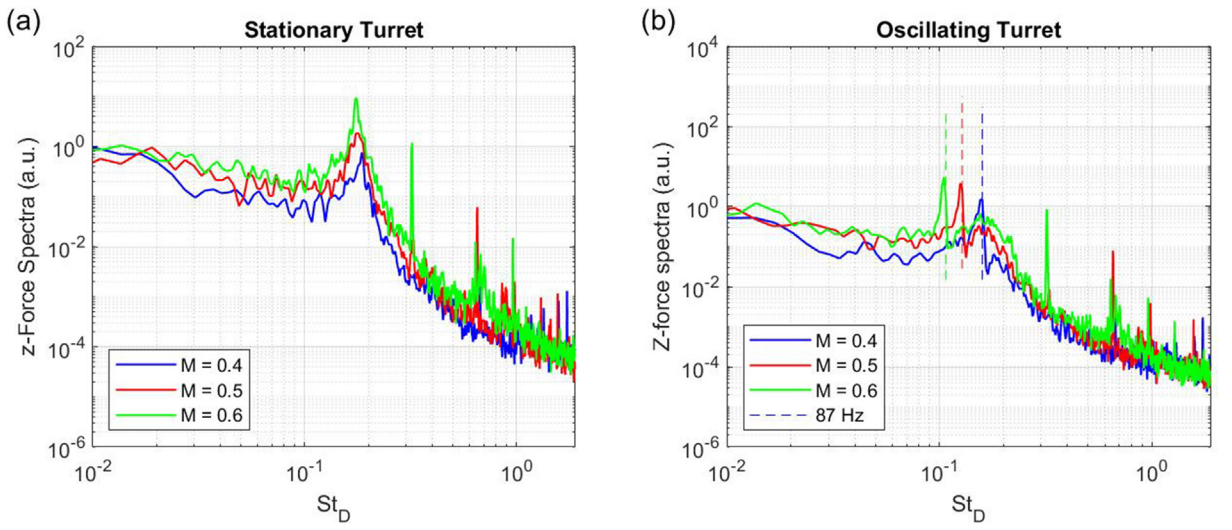

Fig. 17. Spectra of z-component of fluctuating force for (a) the stationary turret, and (b) the oscillating turret, at $M = 0.4$, 0.5 and 0.6. In plot (b), the main oscillating frequency of 87 Hz is indicated as colored vertical dashed lines.. (For interpretation of the references to color in this figure legend, the reader is referred to the web version of this article.)

direction and the resulted work produced by the flow will reduce the pressure and, consequently, the z-force, acting on the oscillating turret. Since the turret cannot move in the streamwise direction, the turret motion does not affect the streamwise force.

Spectra of the spanwise z-component of the unsteady force on the oscillating and stationary cases are presented as a function of the normalized frequency at $M = 0.4$, 0.5 and 0.6 in Fig. 17. For the stationary case, see Fig. 17(a), the spectrum of z-force has a broad peak at the same normalized frequency of $St_D = 0.17$, the location of this spectral peak is independent of the Mach number. In contrast, the dominant peak, present in the z-force for the oscillating turret, see Fig. 17(b), coincides with 87 Hz resonant frequency, indicated as vertical dashed lines. There is a second weaker peak in the spectrum located at the normalized frequency of $St_D = 0.17$, and it appears to be significantly dampened with respect to the stationary case at all Mach numbers. The analysis of spectra for other force components were not significantly affected by the oscillating turret, see Roeder (2020) for details.

To investigate the intermittent nature of the spanwise z-force, a Morlet wavelet analysis was applied to the time series of the spanwise force coefficient for the stationary and the oscillating cases at $M = 0.5$. A map of wavelet amplitude for the stationary case as a function of the normalized frequency and normalized time is shown in Fig. 18(a). The force amplitude is clearly intermittent, with a typical burst durations of 20–40 D/U_∞; similar time durations of the wake coherence around the hemisphere were observed in McCarthy et al. (2019). Most of the force bursts occur at the range of $St_D = 0.1$–0.25, so some of the bursts would coincide with the natural resonant frequency of 87 Hz, indicated in Fig. 18(a) as a horizontal dashed white line. When it happens, the oscillating turret will responds to these force bursts by amplifying the turret motion. When the force burst either shifts away from the resonant 87 Hz or decreases in amplitude, the turret motion is dampened. For this reason, the observed bursts in the force are very similar to the bursts in the turret motion observed in Fig. 7.

As it was demonstrated in Fig. 17, due to aero-elastic interaction, the turret motion will modify the spectrum of the spanwise force by suppressing the natural peak at $St_D \sim 0.17$ and enhancing the spectral energy at the fixed resonant frequency of 87 Hz. This effect can be observed in the wavelet map for the oscillating case in Fig. 18(b), where most of the force bursts now occur near 87 Hz. The durations of the bursts appear to be unchanged, while the frequency and the amplitudes of the burst occurrences are reduced, compared to the stationary case. These less frequent and less energetic bursts result in the overall reduced values of the spanwise force coefficients, reported in Fig. 16.

Finally, using the computed unsteady force in the z-direction, F_z, and the resulting turret position, z_{turret}, it is possible to extract the spectral transfer function between these quantities as a ratio of Fourier transforms, $G(f) = FT\{F_z\}/FT\{z_{turret}\}$, and to compare it with the theoretical transfer function, Eq. (4). The amplitude and the phase of the experimentally calculated transfer function, normalized by the steady value of the transfer function, G_{steady}, are presented in Fig. 19, along with the theoretical transfer function. These results agree quite well with the linear second-order model up to 150 Hz, including the location and the amplitude of the resonant peak, as well as the phase jump, verifying that the turret motion can be approximately modeled as a linear second-order underdamped system. Above 150 Hz, the experimental transfer function deviates from the linear model. One reason for it is possible non-linear effects of these high frequencies; similar non-linear effects were observed in the spectra of the turret position in Fig. 6. Another reason is that the spectrum of the turret position, presented in Fig. 6 is essentially flat for frequency above 100 Hz due to the noise related to accuracy of the optical technique to extract the turret position.

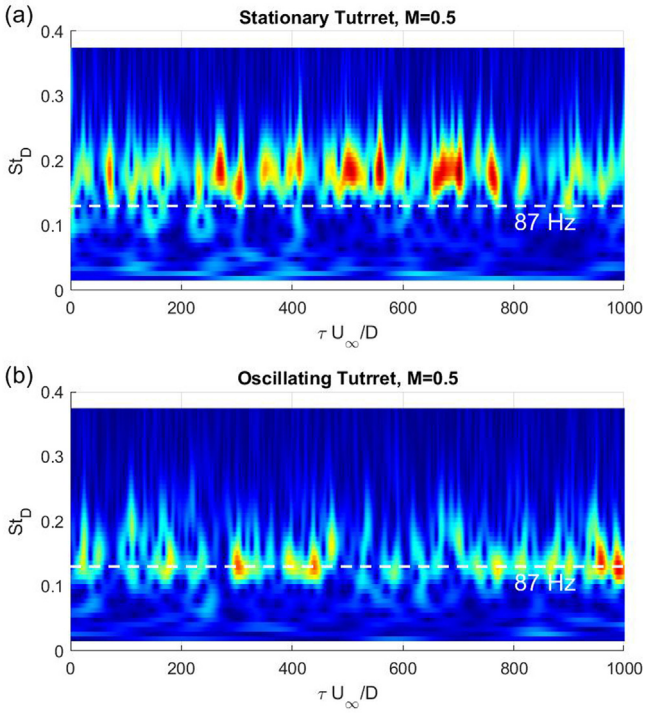

Fig. 18. Amplitude of Morlet wavelet transform of the spanwise fluctuating force for (a) stationary turret and (b) oscillating turret cases at $M = 0.5$. The main oscillating frequency of 87 Hz as marked by a dashed white line.

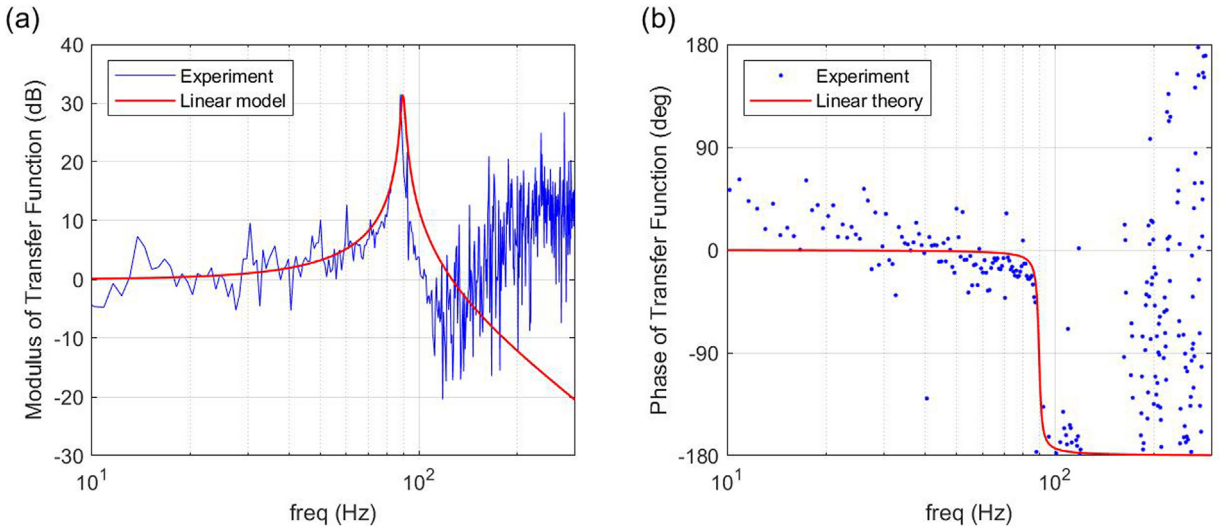

Fig. 19. (a) Amplitude and (b) phase of experimentally-measured harmonic normalized transfer function, $G(f)/G_{\text{steady}}$, between the unsteady z-force and the resulted turret z-displacement at $M = 0.5$. The theoretical linear model from Eq. (4) is also shown for comparison.

6. Conclusions

In the presented studies, the oscillating turret assembly has been designed, built and experimentally tested in a subsonic tunnel over a range of Mach numbers between 0.3 and 0.6 at high Reynolds numbers of $1.7 \times 10^6 \leq Re_D \leq 2.6 \times 10^6$. The hemispherical turret is mounted on a thin aluminum beam, allowing the turret to freely move in the spanwise direction only. Only the hemispherical turret was inserted into the flow. The oscillating turret was designed using Euler–Bernoulli beam theory to oscillate at a predominantly single resonant frequency. The parameters of the mounting

beam were tuned for the oscillating frequency to lie inside the wake-dominant frequency of $St_D \sim 0.17$, so the resonant aero-elastic interaction would result in forced turret oscillations.

The optical-based measurements confirmed that the turret oscillations were confined to the spanwise direction only. The time-resolved turret motion showed that the turret oscillated in bursts of pseudo-periodic motion, where the turret exhibited relatively stationary regime followed by periods of strong oscillations at a fixed frequency. The durations of these periods of the oscillatory turret motion were found to be on the order of 100–200 D/U_∞.

An extensive study using pressure-sensitive paint (PSP) was conducted in order to investigate the globally-reconstructed fluctuating pressure fields on and around both oscillating and stationary turrets. The spatial distributions of the pressure coefficient in the wake indicate that flow-induced turret oscillations suppress the total surface pressure energy and increase the wake size at all tested Mach numbers. Analysis of the surface convective velocities around the turret linked the local increases in the fluctuating pressure to the unsteady necklace vortex in front of the turret and near the unsteady re-attachment line in the wake. The analysis also confirmed the increased wake size for the oscillating turret. A conditional analysis of the pressure fields during the stationary and the pure oscillating regimes for the oscillating case using a Morlet wavelet transform showed that the pressure spatial distribution in the wake is essentially the same during these different regimes, indicating long response times of the turret wake.

JPOD modal analysis was applied in order to investigate the spatial distribution and the spectra of the different wake modes for the oscillating and the stationary cases. It was found that the spanwise anti-symmetric modes have a sharp peak at $St_D \sim 0.17$, and this peak was substantially suppressed for the oscillating case at all tested Mach numbers. The spanwise-symmetric modes corresponding to the global symmetric motion, were found to be mostly unaffected by the turret motion. Therefore, the mechanical motion of the oscillating turret was responsible for the reduction of the overall pressure fluctuation of the wake by suppressing the global anti-symmetric wake motion. The results can be logically interpreted in the context of energy conservation, where the energy in the wake must be reduced in order for the flow to do work on the oscillating turret.

Due to aero-elastic interaction, the anti-symmetric wake motion was dynamically locked with the mechanical motion of the oscillating turret. An analysis of unsteady forces acting of the turret itself revealed that the largest unsteady forcing for both turret configurations occurs in the spanwise direction. The unsteady force spectra showed that the dominant frequency corresponded to the resonant oscillating frequency for the oscillating turret and the dominant wake response frequency for the stationary turret. The spanwise unsteady force was also demonstrated to be intermittent in time, explaining the bursts of the periodic turret motion for the oscillating case. The spectral transfer function, extracted from the simultaneous force and the resultant turret motion, agree reasonably well with the prediction from the linear second-order underdamped model.

The presented work can be useful to interpret the changes in the turret wake and in the unsteady forces acting on the turret due to aero-elastic effects and can be used to validate numerical codes, capable of solving the coupled aero-elastic response and aero-dynamic performance of the hemispherical turrets.

CRediT authorship contribution statement

Aaron L. Roeder: Methodology, Data curation, Software, Writing – original draft, Reviewing and editing. **Stanislav Gordeyev:** Conceptualization, Funding acquisition, Project administration, Supervision, Methodology, Software, Writing – original draft, Reviewing and editing.

Declaration of competing interest

The authors declare that they have no known competing financial interests or personal relationships that could have appeared to influence the work reported in this paper.

Acknowledgments

This work is supported by the Air Force Research Laboratory, United States, Cooperative Agreement number FA9451-17-2-0088. The U.S. Government is authorized to reproduce and distribute reprints for governmental purposes notwithstanding any copyright notation thereon.

The authors would like to thank Dr. Hirotaka Sakaue and Daiki Kurihara for their invaluable help in setting up and conducting PSP experiments and in reducing PSP data.

Disclosures

Approved for public release; distribution is unlimited. Public Affairs release approval # AFRL-2021-0921.

References

Bearman, P.W., 2011. Circular cylinder wakes and vortex-induced vibrations. J. Fluids Struct. 27, 648–658. http://dx.doi.org/10.1016/j.jfluidstructs.2011.03.021.

Coirier, W.J., Porter, C., Barber, J., Stutts, J., Whiteley, M., Goorskey, D., Drye, R., 2014. Aero-optical evaluation of notional turrets in subsonic. Transonic Supersonic Regimes. AIAA Pap. 2014–2355.

De Lucca, N., 2015. Studies of the Pressure Field and Related Beam Jitter for Hemisphere-on-Cylinder Turrets University of Notre Dame.

De Lucca, N., Gordeyev, S., Jumper, E.J., 2013a. In-flight aero-optics of turrets. J. Optical Engineering 52 (7), 071405. http://dx.doi.org/10.1117/1.OE.52.7.071405.

De Lucca, N., Gordeyev, S., Jumper, E.J., Hird, K., Juliano, T.J., Gregory, J.W., Thordahl, J., Wittich, D.J., 2013b. The estimation of the unsteady aerodynamic force applied to a turret in flight. AIAA Pap. 2013–3136.

De Lucca, N., Gordeyev, S., Morrida, J., Jumper, E.J., 2018a. Investigation of flow dynamics over turrets with different spanwise aspect ratios using PSP. AIAA Pap. 2018–2047.

De Lucca, N., Gordeyev, S., Morrida, J., Jumper, E.J., Wittich, D.J., 2018b. Modal analysis of the surface pressure field around a hemispherical turret using pressure sensitive paint. AIAA Pap. 2018-0932.

Erturk, A., Inman, D.J., 2011. Piezoelectric Energy Harvesting, first ed. John Wiley & Sons Ltd.

Gordeyev, S., De Lucca, N., Jumper, E.J., Hird, K., Juliano, T.J., Gregory, J.W., Thordahl, J., Wittich, D.J., 2014. Comparison of unsteady pressure fields on turrets with different surface features using pressure-sensitive paint. Exp. Fluids 55, 1661. http://dx.doi.org/10.1007/s00348-013-1661-9.

Gordeyev, S., De Lucca, N., Morrida, J., Jumper, E.J., Wittich, D.J., 2018. Conditional studies of the wake dynamics of hemispherical turret using PSP. AIAA Pap. 2018–2048.

Gordeyev, S., Jumper, E., 2010. Fluid dynamics and aero-optics of turrets. Prog. Aerosp. Sci. 46, 388–400. http://dx.doi.org/10.1016/j.paerosci.2010.06.001.

Gordeyev, S.V., Thomas, F.O., 1999. Temporal subharmonic amplitude and phase behavior in a jet shear layer: Wavelet analysis and Hamiltonian formulation. J. Fluid Mech. 394, 205–240.

Gordeyev, S., Vorobiev, A., Jumper, E., Gogineni, S., Wittich, D.J., 2016. Studies of flow topology around hemisphere at transonic speeds using time-resolved oil flow visualization. AIAA Pap. 2016-1459.

Hayashi, T., Sakaue, H., 2020. Temperature effects on polymer-ceramic pressure-sensitive paint as a luminescent pressure sensor. Aerospace 7 (6), 80. http://dx.doi.org/10.3390/aerospace7060080.

Jelic, R., Sherer, S., Greendyke, R., 2013. Simulation of various turret configurations at subsonic and transonic flight conditions using OVERLOW. J. Aircr. 2013 50 (2), 398–409. http://dx.doi.org/10.2514/1.C031844.

Jumper, E.J., Gordeyev, S., 2017. Physics and measurement of aero-optical effects: Past and present. Annu. Rev. Fluid Mech. 49, 419–441. http://dx.doi.org/10.1146/annurev-fluid-010816-060315.

Jumper, E.J., Zenk, M., Gordeyev, S., Cavalieri, D., Whiteley, M.R., 2012. The airborne aero-optics laboratory, AAOL. In: Proc. SPIE 8395, Acquisition, Tracking, Pointing, and Laser Systems Technologies XXVI. 839507. http://dx.doi.org/10.1117/12.922734.

Ladd, J., Mani, A., Bower, W., 2009. Validation of aerodynamic and optical computations for the unsteady flow field about a hemisphere-on-cylinder turret. AIAA Pap. 2009–4118.

Lee, T., Lee, C., Nonomura, T., Asai, K., 2020. Unsteady skin-friction field estimation based on global luminescent oil-film image analysis. J. Vis. 23, 763–772. http://dx.doi.org/10.1007/s12650-020-00661-y.

Lee, T., Nonomura, T., Asai, K., Liu, T., 2018. Linear least-squares method for global luminescent oil film skin friction field analysis. Rev. Sci. Instrum. 89, 065106. http://dx.doi.org/10.1063/1.5001388.

Liu, T., Montefort, J., Woodiga, S., Merati, P., Shen, L., 2008. Global luminescent oil-film skin-friction meter. AIAA J. 46 (2), 476–485. http://dx.doi.org/10.2514/2.538.

Liu, T., Shen, L., 2008. Fluid flow and optical flow. J. Fluid Mech. 614, 253–291. http://dx.doi.org/10.1017/S0022112008003273.

Lucas, B.D., Kanade, T., 1981. An iterative image registration technique with an application to stereo vision. In: Proceedings of 7th international joint conference on artificial intelligence, pp. 674–679.

Manhart, M., 1998. Vortex shedding from a hemisphere in a turbulent boundary layer. Theoretical and Computational Fluid Dynamics 12 (1), 1–28. http://dx.doi.org/10.1007/s001620050096.

Matthews, E., Wang, K., Wang, M., Jumper, E., 2016. Les of an aero-optical turret flow at high Reynolds number. AIAA 2016-1461.

McCarthy, J.M., Giacobello, M., Lam, S., 2019. Wavelet coherence of surface pressure fluctuations due to von kármán vortex shedding near a hemispherical protuberance. Exp. Fluids 60 (3), http://dx.doi.org/10.1007/s00348-018-2644-7.

Morgan, P.E., Visbal, M.R., 2012. Hybrid Reynolds-averages Navier–Stokes/large-eddy simulation investigating control of flow over a turret. J. Aircr. 49 (6), 1700–1717. http://dx.doi.org/10.2514/1.C031239.

Morrida, J., Gordeyev, S., De Lucca, N., Jumper, E.J., 2017. Shock-related effects on aero-optical environment for hemisphere-on-cylinder turrets at transonic speeds. Appl. Opt. 56 (16), 4814–4824. http://dx.doi.org/10.1364/AO.56.004814.

Morrida, J., Gordeyev, S., Jumper, E., 2016. Transonic flow dynamics over a hemisphere in flight. AIAA Pap. 2016-1349.

Porter, C., Gordeyev, S., Zenk, M., Jumper, E., 2013. Flight measurements of the aero-optical environment around a flat-windowed turret. AIAA J. 51 (6), 1394–1403. http://dx.doi.org/10.2514/1.J052067.

Repetto, C.E., Roatta, A., Welti, R.J., 2012. Forced vibrations of a cantilever beam. Eur. J. Phys. 33 (5), 1187. http://dx.doi.org/10.1088/0143-0807/33/5/1187.

Roeder, A.L., 2020. An experimental investigation of the wake response downstream of a spanwise-oscillating hemispherical turret. M.S. thesis. University of Notre Dame.

Sarpkaya, T., 2004. A critical review of the intrinsic nature of vortex-induced vibrations. J. Fluids Struct. 19 (4), 389–447. http://dx.doi.org/10.1016/j.jfluidstructs.2004.02.005.

Savory, E., Toy, N., 1986. The flow regime in the turbulent near wake of a hemisphere. Exp. Fluids 4, 181–188. http://dx.doi.org/10.1007/BF00717812.

Taira, K., Brunton, S.L., Dawson, S.T.M., Rowley, C.W., Colonius, T., McKeon, B.J., Schmidt, O.T., Gordeyev, S., Theofilis, V., Ukeiley, L.S., 2017. Modal analysis of fluid flows: An overview. AIAA J. 55 (12), 4013–4041. http://dx.doi.org/10.2514/1.J056060.

Tavakol, M.M., Abouali, O., Yaghoubi, M., 2015. Large eddy simulation of turbulent flow around a wall mounted hemisphere. Appl. Math. Model. 39 (13), 3596–3618. http://dx.doi.org/10.1016/j.apm.2014.11.055.

Vukasinovic, B., Glezer, A., Gordeyev, S., Jumper, E., Bower, W.W., 2013. Flow control for aero-optics application. Exp. Fluids 54, 1492. http://dx.doi.org/10.1007/s00348-013-1492-8.

Wang, M., Mani, A., Gordeyev, S., 2012. Physics and computation of aero-optics. Annu. Rev. Fluid Mech. 44, 299–321. http://dx.doi.org/10.1146/annurev-fluid-120710-101152.

Williamson, C.H.K., Govardhan, R., 2004. Vortex-induced vibrations. Annu. Rev. Fluid Mech. 36, 413–455. http://dx.doi.org/10.1146/annurev.fluid.36.050802.122128.

Wood, J.N., Breuer, M., De Nayer, G., 2018. Experimental studies on the instantaneous fluid–structure interaction of an air-inflated flexible membrane in turbulent flow. J. Fluids Struct. 80, 405–440. http://dx.doi.org/10.1016/j.jfluidstructs.2018.02.006.

Wood, J.N., De Nayer, G., Schmidt, S., Breuer, M., 2016. Experimental investigation and large–eddy simulation of the turbulent flow past a smooth and rigid hemisphere. J. Flow Turbul. Combust. 97 (1), 79–119. http://dx.doi.org/10.1007/s10494-015-9690-5.